Chemical Engineering Journal 498 (2024) 155570

Contents lists available at ScienceDirect

Chemical Engineering Journal

journal homepage: www.elsevier.com/locate/cej

Reaction mechanism of 1,2-dichlorobenzene oxidation over MnO_X-CeO_2 and the effect of simultaneous NO selective reduction

J.A. Martín-Martín [a], A. Aranzabal [a,*], M.P. González-Marcos [a], E. Finocchio [b], J.R. González-Velasco [a]

[a] Group of Chemical Technologies for Environmental Sustainability, Department of Chemical Engineering, Faculty of Science and Technology, The University of the Basque Country, UPV/EHU, P.O. Box 644, E-48080 Bilbao, Spain

[b] Dipartimento di Ingegneria Civile, Chimica e Ambientale, Università di Genova, Via Opera Pia 15, I-16145 Genova, Italy

ARTICLE INFO

Keywords:
MnO_X-CeO_2
1,2-dichlorobenzene
In-situ FTIR
Reaction pathway
NO
NH_3

ABSTRACT

MnO_X-CeO_2 formulation has been studied for the catalytic oxidation of 1,2-dichlorobenzene. Among the samples with different Mn and Ce content, the most active was 85%mol Mn and 15%mol Ce, due to its better morphological properties and the synergy achieved between the two phases composing it (mixed oxide phase and segregated Mn oxide). Deactivation was monitored at low temperature and a transient change in the oxidative capability at high temperature because of active sites with different oxidative capability. Based on in-situ FTIR results, oxidation reaction pathway is proposed. Active sites with different oxidative capability causes some reaction steps to occur faster than others as a function of temperature, which modifies the distribution of intermediate species. In the reduction of NO, its adsorption leads to nitrate species contributing to a faster re-oxidation of active sites and the presence of NH_3 promotes the removal of adsorbed Cl.

1. Introduction

Chlorinated volatile organic compounds (CVOCs) and polychlorinated dibenzodioxins (PCDD) and dibenzofurans (PCDF) are hazardous pollutants with high toxicity, due to their high persistence in the environment and strong bioaccumulation risk into the living beings. Therefore, law regulations establishing emission limits for PCDD/Fs are strict.

This type of pollutants is mainly generated in industrial processes involving the combustion of carbon-based compounds with any content of chorine; for example, incineration plants of municipal or medical waste, power plants, sinter plants, cement manufacturing plants, etc. [1]. The conventional technologies for CVOCs and PCDD/Fs abatement include activated carbon injection followed by bag filter, wet scrubbing, catalytic filters and thermal decomposition [2]. The thermal oxidation requires high temperatures, 850–1000 °C, resulting in extra auxiliary fuel costs. Furthermore, incomplete combustion can cause the formation of a variety of harmful by-products. For example, the subsequent formation of PCDD/Fs [3] under start-stop conditions via the route known as novo synthesis is particularly problematic [1,4].

These industrial processes must also afford the destruction of NO_X, generated at high-temperature combustion. Although the commonly used method to reduce the emissions of NO_X has been the injection of NH_3 in the combustion chamber, or even in the flue gas, currently Selective Catalytic Reduction (SCR) technology is the most effective method of NO_X reduction in power generation, waste incinerators and industrial process applications [5].

Catalytic oxidation is proposed as a promising alternative for the abatement of CVOCs pollutants, since it destroys them to CO_2, HCl and H_2O in a much lower temperature range than thermal combustion, that is 250–500 °C. This leads to a higher energy efficiency and avoids the formation of PCDD/Fs by the novo synthesis in the subsequent cooling of exhaust gases. In addition, catalytic oxidation has a notable removal efficiency at very low concentrations of the pollutant, which avoids the use of an additional adsorption stage.

The most studied catalyst compositions for catalytic oxidation and combustion are those based on supported noble metals and transition metal oxides [6]. Noble metal catalysts (mainly Pt and Pd) are reported to have an excellent ability in the oxidation of CVOCs [7–9]. Giraudon and co-workers [10] concluded TiO_2 provides the best catalytic activity after assessing several mesoporous supports. The use of zeolites has also been investigated due to their excellent acid properties, which provide a

* Corresponding author.
E-mail address: asier.aranzabal@ehu.es (A. Aranzabal).

https://doi.org/10.1016/j.cej.2024.155570
Received 12 June 2024; Received in revised form 5 September 2024; Accepted 5 September 2024
Available online 7 September 2024

promotion of oxidative capability and possibly favour desorption of chlorine species. Taralunga and co-workers [11] evaluated several metal-free zeolites and their corresponding Pt supported samples on 1,2-dichlorobenzene (o-DCB) oxidation. They identified H-FAU as the most active zeolite and concluded that Pt increases notoriously the catalytic activity, although also leads to the production of polychlorinated compounds as by-products. Similarly, Scirè and co-workers [12] reported higher catalytic activity of supported Pt over H-ZSM5 compared to H-BETA and Al_2O_3. However, noble metal-based catalysts are quite restricted due to their high cost and the deactivation by chlorine deposition.

On the other hand, within transition metal oxide-based catalysts, VO_X/TiO_2 catalysts have been widely studied for having a higher catalytic activity and stability in the oxidation of chlorinated benzenes, which are commonly used as model compounds of PCDD/Fs [13]. In fact, Corella and co-workers [14] reported to achieve higher o-DCB conversions with V_2O_5-WO_3/TiO_2 than with other catalytic formulations based on noble metals. The excellent catalytic performance of V-based catalysts has also been corroborated in the catalytic oxidation of VOCs, i.e. propane, propene, isopropanol, etc. [15–17], and other CVOCs with oxygenated function, for example chlorophenol and trichlorophenol [18,19].

Vanadium-titanium oxide is the most common composition used by catalyst manufacturers for SCR units. The fact that the same formulation is active for both oxidation of CVOC/PFDD/Fs and reduction of NOx, allows to retrofit the existing incinerators with a catalytic converter unit as in the case of the IVAGO waste incineration plant (Ghent, Belgium) [20] and a sinter plant in Taiwan [21].

The feasibility of eliminating CVOCs and NOx in the same catalytic unit simultaneously, as opposed to the traditional situation of having two separate processes, implies an increase in the efficiency and sustainability for the gas cleaning lines. That is why this option is included in the current document on Best Available Techniques for waste incineration [5]. At lab-level, high levels of simultaneous removal of NO and o-DCB has been also reported in our previous works [22–24] with VO_X/TiO_2 and metal-loaded ZSM5 zeolites.

Recently, Mn-based catalytic formulation has been largely encouraged for carrying out catalytic oxidation reaction, since it is a more environmentally friendly material and has an excellent oxidation ability due to its efficiency in oxidation/reduction cycles [25]. Nonetheless, this type of catalysts is reported to be considerably deactivated by chlorine deposition. Catalytic activity and stability of Mn-based catalysts is improved by the addition of other metals. Among dopant metals, Ce is the most reported in the literature, as it provides high storage and mobility of oxygen into the catalyst structure [26,27]. Then, the behaviour of MnO_X-CeO_2 catalysts has been studied for the oxidation of VOCs, i.e. hexane, phenol and toluene [28–30], and CVOCs, i.e. polychlorinated benzenes and trichloroethylene [31], and in the selective catalytic reduction (SCR) of NO_X at low temperature, with relevant efficiency results [32]. However, the number of papers dealing with simultaneous abatement of CVOCs and NOx over MnO_X-CeO_2 catalyst, is considerably low [33].

To the best of the authors' knowledge, based on an extensive literature review, there are hardly any studies analysing the reaction mechanism of o-DCB (commonly used as a model compound of PFDDs at laboratory research) oxidation on MnO_X-CeO_2 by in-situ FTIR experiments and, even less in the situation where o-DCB oxidation takes place in the presence of NO and NH_3 on MnO_X-CeO_2, as an alternative to the current technology in some incineration processes.

Then, the objective of this work is to advance in the knowledge of the reaction pathway of o-DCB oxidation over MnOx-CeOx catalysts specifically, both in the absence of NOx and in the presence of NOx. Five samples of catalysts with different Mn/Ce proportions have been prepared, characterized and tested in the oxidation of o-DCB, with the aim to determine what type of catalyst properties are relevant, in terms of activity and durability. In-situ FTIR experiments have been carried out with the aim to determine the reaction mechanism of the oxidation of o-DCB, in the absence and in the presence of NO_X selectively reduced with NH_3.

2. Experimental

2.1. Catalyst preparation

MnO_X-CeO_2 catalysts were prepared by co-precipitation method. The right amount of precursor compounds, $Mn(NO_3)_2{\cdot}4H_2O$ and $Ce(NO_3)_3{\cdot}6H_2O$, was added to distilled water at room temperature. Then, the precipitation of active metals, Mn and Ce, was carried out by pouring drop by drop a solution of $H_2NCOONH_4$ 1.3 M until reaching a pH value of 9. After aging the resulting suspension for 2 h, it was filtered and washed with distillate water. Finally, the solid was dried overnight and calcined in static air at 500 °C for 3 h with a heating ramp of 1 °C/min. Three bimetallic samples were prepared with 15, 50 and 85 % mol Mn, named 15Mn85Ce, 50Mn50Ce and 85Mn15Ce, respectively. In order to avoid mass transfer limitations, all the samples were sieved to 0.3–0.5 mm.

2.2. Catalyst characterization

X-ray diffraction (XRD) analysis was carried out on a Philips PW 1710 X-ray diffractometer with Cu Kα radiation ($\lambda = 1.5406$ Å) and Ni filter. The measurements were done with a step size of 0.026° and a counting time of 528 s in the 2θ range of 20 and 60°. The diffraction peaks were associated to the corresponding crystal phases by comparing with JCPDS database cards.

Raman spectroscopy was carried out in a Renishaw System 1000 Raman spectrometer. As excitation source, a 706 nm solid-state laser was used, with a power of 1 mW. The measurements were made at room temperature.

N_2 adsorption–desorption was performed on a Micromeritics TRISTAR II 3020 at −196 °C. The specific surface area and pore volume were calculated by using BET procedure. Before the analysis, the samples were pre-treated at 350 °C for 4 h with a flow of nitrogen.

FT-IR skeletal spectra were recorded by means of a Nicolet Nexus instrument on disk of catalytic powders diluted in KBr (around 1 % in weight). Additionally, the spectra of the catalyst pure powders were recorded by self-supporting disks of catalytic powders placed in the IR cell, and connected to a gas manipulation apparatus. The disks were previously activated at 500 °C in vacuum (10^{-3} torr). The spectra were collected by 100 scans with a resolution of 4 cm^{-1} resolution.

Temperature programmed reduction with H_2 (H_2-TPR) was carried out on a Micromeritics AutoChem 2920 instrument. The analysis was done by heating the sample (15–20 mg) from 100 to 900 °C with a heating ramp of 10 °C/min in a continuous flow of 5 % H_2/Ar (50 cm^3/min). The H_2 consumption was monitored with a TCD. A cold trap was used to capture water and avoid its interference on TCD. Before the analysis, the samples were pre-treated at 500 °C for 45 min with a continuous flow of 5 % O_2/He (50 cm^3/min).

Thermogravimetric analysis (TGA) analysys was used to analyse the deactivating species adsorbed on the used catalysts. The experiments were performed in a Setaram Setsys Evolution thermobalance with a cylindrical graphite furnace and an alumina crucible. This equipment was coupled with a mass spectrometer Pfeitffer Vacuum DUO 2.5 in order to identify the gaseous products of the experiment. To avoid the desorption of deactivating species and only remove ambient adsorbed molecules, the sample was subjected to a low temperature pretreatment, 120 °C, with a 50 mL/min of 5 % O_2/He stream for 30 min. Then, the experiment was carried out with the same stream and increasing temperature with a heating rate of 5 °C/min up to 500 °C, temperature which was kept constant for 3 h.

SEM-EDS was used to obtain information about surface concentration of deactivated catalysts. It was performed on a Carl Zeiss EVO-40

scanning electron microscope coupled with X-Max EDS from Oxford Instruments. The operating conditions during the measurements were 30 kV and 180 pA.

2.3. Reaction set-up and catalytic tests

Fig. 1 shows a flow diagram of the reaction set-up. Oxidation reaction of o-DCB (used as a model compound of PCDD/Fs) was carried out on a quartz reactor with an inner diameter of 14 mm located inside a convective oven. The catalytic bed, with a total volume of 3 cm^3, was composed by 1.5 g of sieved catalyst between 0.3–0.5 mm and inert quartz sieved between 0.5–0.8 mm. All the catalytic tests were carried out with a feeding flow rate of 2 L_N/min (GHSV 40000 h^{-1}) and at a pressure of 1.5 atm. Before each experiment, the catalytic bed was exposed to 2 L_N/min of Ar at 200 °C for 2 h as a pretreatment.

Catalytic activity tests for the selection of the most active MnO_X-CeO_2 catalyst in o-DCB oxidation were carried out by light-off experiments increasing reaction temperature from 100 to 450 °C (heating ramp of 1.5 °C/min) and with a feeding stream composed by o-DCB (100 ppm), O_2 (10 %) and Ar to balance. Stability tests were carried out with Time-on-Stream (TOS) experiments at 200 and 300 °C, keeping constant these temperatures for 24 h. The effect of reactants involved in NO reduction on o-DCB oxidation was evaluated by two types of experiments. On the one hand, with a light-off experiment similar to that above described, but with a feeding stream composed by o-DCB (100 ppm), O_2 (10 %), NO (300 ppm), NH_3 (300 ppm) and Ar to balance. On the other hand, with transient experiments in which o-DCB oxidation was performed in the presence of NO or NH_3. In this latter, the NO or NH_3 concentration ranged from 0 to 600 ppm.

o-DCB was the only reactant fed as liquid and its flow was regulated by a mass flow controller (Bronkhorst® High-Tech μ-Flow L01-AAA-99-0-20S). The feeding of the remaining gaseous reactants was also controlled by mass flow controllers (Bronkhorst® High-Tech F-201CV). The feeding system has a controlled-evaporator-mixer (Bronkhorst® High-Tech W-102A-111-K) and electrical resistances for heating all pipes to ensure the complete evaporation of o-DCB. The gaseous stream before and during the catalytic activity tests was analysed by using, on the one hand, a gas chromatograph (Agilent Technologies 7890A) with a mass selective detector (Agilent Technologies 5975C) for o-DCB and chlorinated organic compounds. A sample of the gas stream is trapped in a loop (0,25 cm^3) connected a single 6-port valve, through which the gas carrier (He) brings the sample, every time the valve changes position, into GC equipped with a HP-VOC capillary column. On the other hand, an ABB Uras 26 Infrared analyser measures continuously the concentration of CO and CO_2 and subsequently an ABB Limas 21 Ultraviolet analyser measures continuously the concentration of NH_3 and NO. o-DCB conversion was calculated according to Equation (1) and CO_2 and CO selectivity through Equations (2) and (3), respectively.

$$X_{oDCB} = \frac{C_{o-DCB,in} - C_{o-DCB,out}}{C_{o-DCB,in}} \cdot 100 \quad (1)$$

$$S_{CO_2} = \frac{C_{co_2,out}}{6 \cdot (C_{o-DCB,in} - C_{o-DCB,out})} \cdot 100 \quad (2)$$

$$S_{CO} = \frac{C_{co,out}}{6 \cdot (C_{o-DCB,in} - C_{o-DCB,out})} \cdot 100 \quad (3)$$

Analysis of both HCl and other chlorinated inorganics, such us Cl_2, ClO_2 and chloramines was performed by bubbling the flow at the reactor exit through a 0.0125 M NaOH solution. Then Cl_2, ClO_2 and chloramines concentration was determined by titration with ferrous ammonium sulphate (FAS) using N,N-diethyl-p-phenylenediamine (DPD) as indicator [7]. For the quantification of each chlorinated inorganics, three samples have been titrated, so that the contribution of each chlorine species can obtained by using a suitable pH (6.2–6.5), additive (KI) and a masking agent (glycine). Chloride ions from HCl(g) in the bubbled solution were measured by Ion Chromatography technique, because the potentiometric method (ion selective electrode), that was suggested initially, showed high experimental error.

Absence of diffusion resistances has been checked by Mears criterion for external mass transfer ($1.3 \cdot 10^{-2} < 0.15$ at 300 °C) and by Weisz-Prater criterion for internal mass transfer ($0.79 < 1$ at 250 °C). Plug flow conditions have been also cheeked by criterion D/d_{pt} (40) > 10 and criterion L/d_{pt} (27.2) $> 20n/Bo \cdot \ln(1/(1-x))$ ($4 \cdot 10^{-3}$), were D is reactor inner diameter, L is bed's length, d_{pt} is catalyst particle size, n is reaction order (1) and Bo is Bodenstein number. Reproducibility of the reaction tests in the experimental setup was measured by regularly repeating the same reaction light-off test over a control catalyst sample. Fig. 2 shows

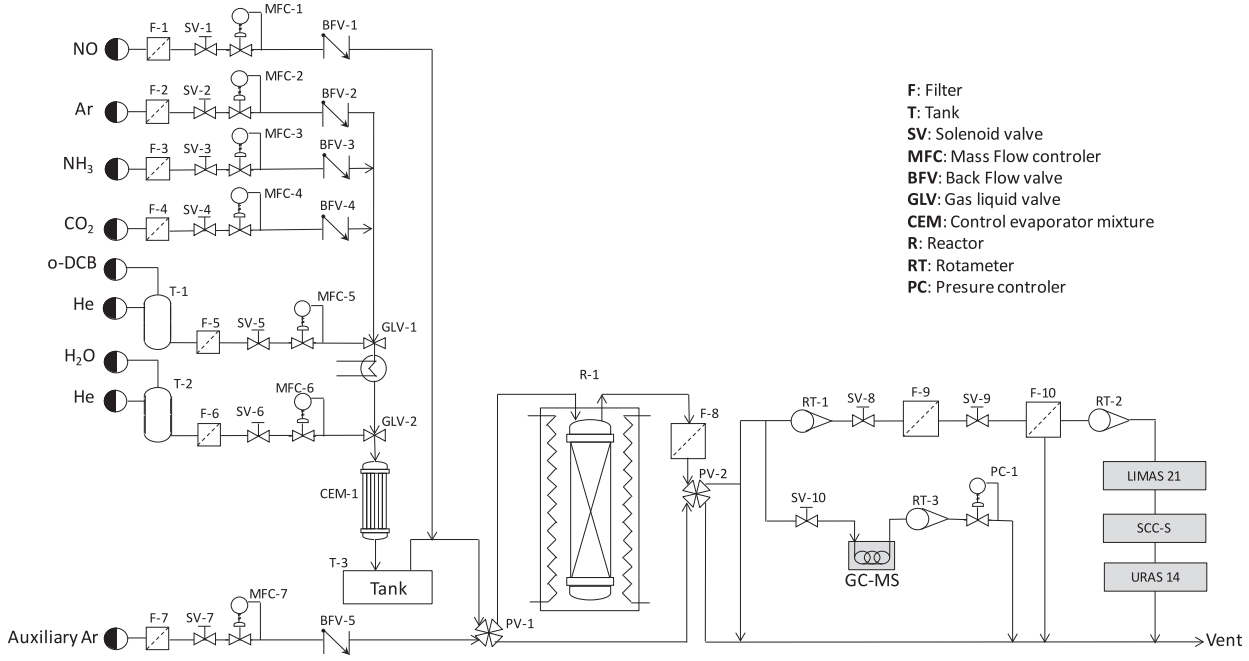

Fig. 1. Experimental set-up for the catalytic tests.

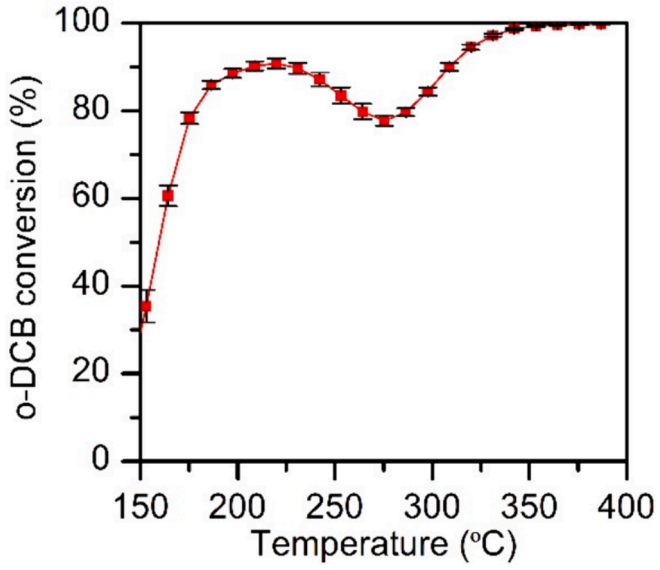

Fig. 2. o-DCB conversion profile with error bars resulting from repeatability tests in the experimental set-up. Reaction conditions: $2l_N$/min, 1.5 atm, 1.5 °C/min, o-DCB (100 ppm), O_2 (10 %) and Ar to balance.

the mean and the standard error of o-DCB measured at selected temperatures. It is important to note that, in all the temperature range, the experimental error is within ±5 %.

2.4. In-situ FTIR analysis

In-situ FTIR experiments were conducted in a Cary 600 Series FTIR spectrometer (Agilent) coupled with a high temperature high pressure (Specac) cell with ZnSe windows. The sample, approximately 50 mg, is pressed into a self-supported disk and placed on a holder inside the cell. Moreover, the experimental set-up is coupled to a vacuum system that allows to generate vacuum in the cell. All the spectra were collected by 48 scans with a resolution of 4 cm^{-1}. Prior to the experiments, the sample is pretreated with a feeding stream of 5 % O_2/Ar (600 mL/min) at 500 °C for 30 min. After that, this stream is by-passed, and the gas cell is subjected to vacuum conditions for 30 min. Then, the gas cell is cooled down to the temperature at which the experiment is to be performed in vacuum conditions. At this point, a spectrum of the clean surface is recorded and will be subtracted of the following spectra recorded during the adsorption experiment.

The adsorption experiments start by flowing the feeding stream into the gas cell. Spectra are recorded as a function of exposure time. After 30 min of exposure time, the weakly adsorbed species are removed by passing 600 mL/min of Ar to the cell. For the analysis of o-DCB adsorbed species, two different feeding streams of 600 mL/min were used in the absence of oxygen (1000 ppm o-DCB and Ar to balance) and in the presence of oxygen (1000 ppm o-DCB, 5 % O_2 and Ar to balance).

On the other hand, the influence of NO and NH_3 adsorbed species on o-DCB oxidation was evaluated by transient experiments. For that purpose, after pre-treatment, the catalyst was firstly exposed to a feeding stream (600 mL/min) composed by 1000 ppm NO and Ar to balance, or 1000 ppm NH_3 and Ar to balance. Then, the NO and NH_3 weakly adsorbed species were removed by flowing Ar. Finally, the catalyst was exposed again to a feeding stream (600 mL/min) composed by 1000 ppm o-DCB and Ar to balance.

3. Results and discussion

3.1. Catalyst characterization

In this section, characterization results of five samples having different Mn/Ce proportions are shown and analysed, with the aim to determine what type of catalyst properties are relevant in the oxidation of o-DCB.

Fig. 3 allows comparing the XRD patterns of samples with different Mn and Ce and the patterns of pure cerium and manganese oxides. Pure cerium oxide exhibits intense diffraction peaks at 28.7, 33.3, 47.7 and 56.6°, characteristic CeO_2 with fluorite crystal phase, whereas the most intense peaks of pure manganese oxide at 33.2, 38.4, 45.4, 49.5 and 55.4° point out that α-Mn_2O_3 is the only crystal phase present in this sample.

Regarding bimetallic samples, the diffraction pattern of the catalyst with the lowest Mn content (15Mn85Ce) shows the presence of diffraction peaks related to fluorite-like structured phase, although they are less intense and broader compared to pure cerium oxide. This trend becomes more noticeable with the further increase in Mn content (50Mn50Ce) and denotes a change of fluorite type crystal domains. This result agrees to the fact that the increase in Mn content causes a decrease in the fluorite crystal size (Table 1), which was estimated by Scherrer equation applied to (1 1 1) plane. This plane corresponds to the most intense XRD peak of Mn_2O_3 phase (at 34° in Fig. 3).

Table 1 also reports the lattice parameter of the crystalline phase. The decrease in the value of the lattice parameter with Mn content suggests that the deterioration in the crystallinity of fluorite phase is due to distortion as a consequence of Mn incorporation into CeO_2 structure, which leads to a solid solution or a mixed oxide phase. In fact, the absence of the diffraction peaks corresponding to other crystalline phase of manganese oxide in the 15Mn85Ce and 50Mn50Ce samples denotes that a great amount of Mn is incorporated to fluorite and, consequently, highly interacting with Ce.

On the other hand, the diffraction pattern of the sample with the

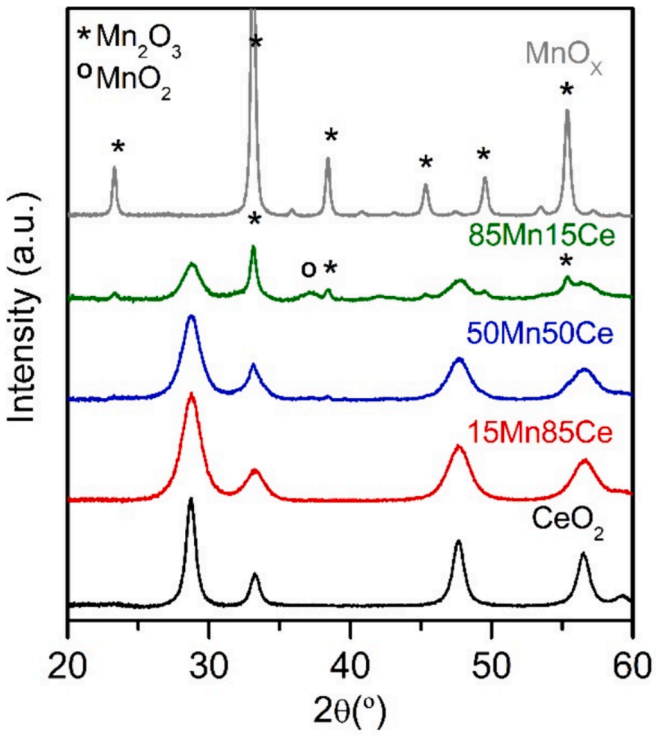

Fig. 3. XRD patterns of MnO_X-CeO_2 samples, measured a step size of 0.026° and a counting time of 528 s in the 2θ range of 20 and 60°.

Table 1
Structural, textural and redox properties of MnOX-CeO2 samples.

Sample	Fluorite Crystal size (nm)	Fluorite lattice parameter (nm)	S_{BET} (m^2/g)	V_{poro} (cm^3/g)	Mn oxidation state
CeO_2	9	5.4135	80	0.12	–
15Mn85Ce	5	5.4054	84	0.18	4.1
50Mn50Ce	4	5.4035	88	0.21	3.5
85Mn15Ce	4	5.4107	87	0.25	3.3
MnO_X	–	–	34	0.17	3.1

highest Mn content (85Mn15Ce) evidences the coexistence of two main crystal phases, fluorite-type and Mn_2O_3, although a small peak at 37.2° also denotes the presence of some MnO_2 phase. The lattice parameter of this sample is lower than that of pure cerium oxide, but higher than those estimated for 15Mn85Ce and 50Mn50Ce catalysts. This corroborates the coexistence of fluorite-type structure partially substituted with Mn and segregated Mn oxide.

Spectroscopies were also used to characterize structural properties. Fig. 4A shows the Raman spectra of bimetallic samples and pure cerium and manganese oxides. The spectrum of pure cerium oxide is characterized by a strong band at 460 cm^{-1} associated to oxygen lattice vibrations, namely F_{2g} mode of the fluorite-type phase. Pure manganese oxide has three broad bands around 695, 640 and 305 cm^{-1} related to ν_7, ν_6 and ν_2 lattice vibrational modes of α-Mn_2O_3.

F_{2g} band is found in the spectra of 15Mn85Ce and 50Mn50Ce catalysts, although it is less intense, broader and shifted towards lower wavelengths compared to pure cerium oxide. It is well known that F_{2g} band is very sensitive to the structural environment of Ce atoms, so this result corroborates the deterioration of fluorite phase above evidenced by XRD as a consequence of Mn incorporation into the CeO_2 structure. In addition, the spectra of those samples exhibit a broad band around 600 cm^{-1}. This band is reported in the literature to be related to oxygen vacancies in the ceria lattice, which are generated as a compensation of the negative charge produced by the incorporation of a doping cation with different nature and oxidation state. Oxygen vacancies promote a faster oxygen mobility and storage along the lattice structure of the catalyst, so their presence plays a key role on the catalytic activity.

On the other hand, the maximum deterioration degree of fluorite phase at high Mn content is observed in the spectrum of 85Mn15Ce catalyst, in which F_{2g} band practically vanishes. For this sample, the most intense band is located at 645 cm^{-1} and is associated to segregated manganese oxide. This result supports the Mn segregation due to the saturation of fluorite phase above observed in XRD. FT-IR skeletal spectra (Fig. 4B) also confirm the smooth transition of the mixed samples structure from the pure ceria lattice, characterized by a main band centered below 500 cm^{-1} (fluorite-type structure) and tailing to 700 cm^{-1}, to the Mn_2O_3 lattice, characterized by a complex Mn-O absorption with three maxima at 669, 575 and 520 cm^{-1}. The spectrum of the 15Mn85Ce sample is close to the spectrum of pure ceria, whose structure is not significantly affected by Mn addition. The spectrum of the 85Mn15Ce sample clearly shows vibrational modes assigned to pure MnO_X, supporting the presence of segregated MnO_X phase also evidenced by XRD. Moreover, the comparison with the spectrum of pure manganese oxide evidences some differences such as the slight shift of the band at 660 cm^{-1} and the disappearance of the shoulder at 500 cm^{-1} that could be related to the modification of Mn-O by the presence of solid solution phase too.

Morphological properties were assessed by N_2-physisorption. According to IUPAC classification, the samples have a mesoporous morphology corresponding to type IV isotherms, as reported elsewhere [34]. The values of surface area and mean pore volume are reported in Table 1. The higher surface area and pore volume of bimetallic samples compared to pure oxides denotes that structural defects caused by Mn incorporation to CeO_2 structure improve the morphology of the catalysts. It is well known that the higher the surface area, the higher the number of exposed active sites leading to a positive impact on catalytic activity. FT-IR analysis of the pure powdered activated surfaces (Fig. 5) evidences that addition of Mn leads to relevant changes of surface hydroxy groups. Pure ceria activated at such mild temperatures is characterized by isolated OHs and bridging OHs showing a quite complex IR pattern with a shoulder at 3700 cm^{-1}, assigned to monocoordinated OH species, and maxima at 3640 cm^{-1} (split, assigned to bridging OH species) and 3500 cm^{-1} (assigned to residual oxo-hydroxide species) [35]. Addition of Mn leads to a decrease in intensity of these bands (15Mn85Ce) and, finally, to a complete change of features in this

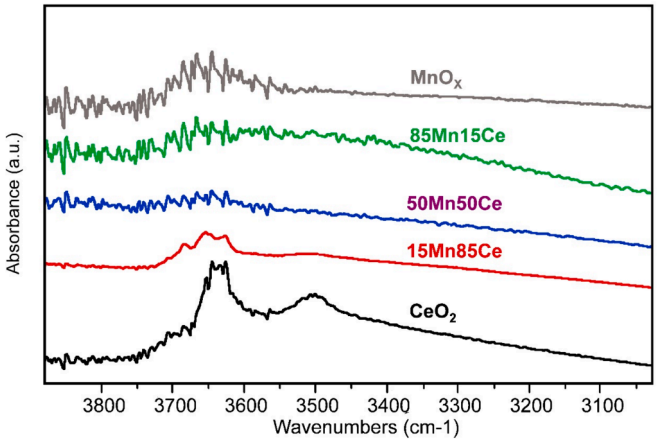

Fig. 5. FT-IR spectra of powder catalysts on a disk diluted in KBr (around 1 % in weight), with data by 100 scans with a resolution of 4 cm^{-1} resolution.

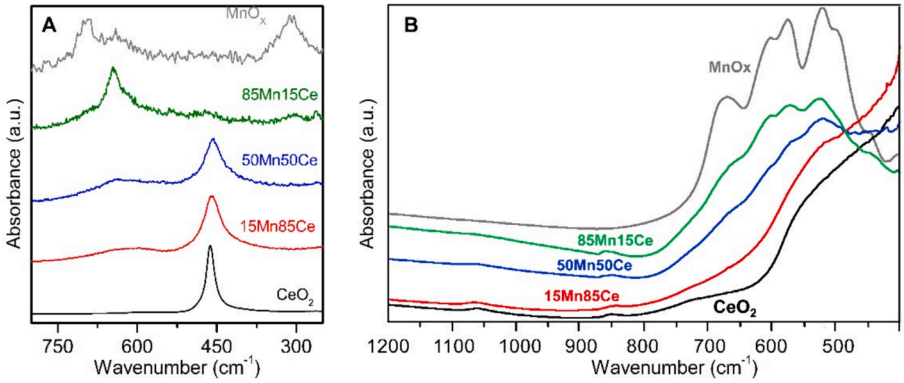

Fig. 4. Raman spectra (A) and FT-IR skeletal spectra (B) of MnOX-CeO2 samples and pure cerium and manganese oxides. Conditions: a 706 nm solid-state laser was used, with a power of 1 mW, measured at room temperature.

spectral region for samples 85Mn15Ce and 50Mn50Ce. In the 85Mn15Ce sample, no isolated species are detected. The surface of this sample is characterized by a weak and broad absorption centred at 3650 cm^{-1} and tailing towards lower frequencies, similar to the band detected in the pure MnO_X spectrum, indicating an extended network of H-bonds. Clearly, Mn addition affects surface hydroxyl groups and, at the highest content, isolated ceria OHs disappear.

Redox properties were studied by H_2-TPR, and the reduction profiles of the samples are shown in Fig. 6. Pure cerium oxide has a reduction profile characterized by two broad peaks around 450 and 800 °C associated to the reduction of surface and bulk Ce, respectively. The quantitative measuring shows that in the sample of pure CeO_2, that H_2 consumption occurs mostly at high temperature, which is associated with the CeO_2 bulk The reduction profile of pure manganese oxide, with two notable peaks around 295 and 425 °C, matches with the reduction of Mn_2O_3. This fact agrees with XRD results where α-Mn_2O_3 was the only crystal phase identified. The reduction peak at lower temperature is related to the reduction of Mn_2O_3 to Mn_3O_4 and the other reduction peak above 400 °C is related to the reduction of Mn_3O_4 to MnO.

Compared to pure oxides, the reduction profiles of bimetallic catalysts are shifted towards lower temperatures. This result indicates that Mn incorporation into Ce structure improves the reducibility of these samples by means of the promotion of oxygen mobility. The sample with the lowest Mn content, 15Mn85Ce, has a similar reduction profile to that of pure cerium oxide, but with two additional reduction peaks. The former, at 100 °C, is associated to the reduction of Mn highly dispersed on the catalytic surface. The latter, around 300 °C, is associated to reduction of both Mn incorporated into CeO_2 lattice and surface Ce.

The increase in Mn content leads to the appearance of two strong reduction peaks around 280 and 400 °C in the 50Mn50Ce and 15Mn85Ce catalysts. These peaks are mainly associated to the reduction of different Mn species. Interestingly, the reduction peak at lower temperature is itself composed by two contributions that are proposed to be associated to the reduction of Mn in different phases. Those phases would correspond to Mn embedded into CeO_2 lattice and segregated Mn, which were clearly identified by XRD. The contribution at lower temperature is proposed to be associated to the reduction of Mn embedded into CeO_2 lattice, because Mn in high interaction with Ce leads to oxygen vacancies that improve reducibility, whereas the other contribution is related to the reduction of segregated Mn.

The average oxidation state of Mn, reported in Table 1, has been estimated from total H_2 consumption and considering some assumptions: MnO is the final Mn reduction state and the H_2 consumption of surface Ce is negligible. As it can be seen, the oxidation state of Mn decreases from Mn^{4+} to Mn^{3+} with Mn content. This result shows that the different phases composing the samples lead to different oxidation state of Mn corresponding to two different contributions in the reduction peaks located at lower temperature. The fact that the contribution of Mn^{4+} species is larger at low Mn content, where all Mn is practically incorporated into CeO_2 structure, indicates that Mn^{4+} species are promoted when Mn is in high interaction with Ce. On the contrary, Mn^{3+} species are promoted at high Mn content due to Mn segregation as Mn_2O_3.

All these characterization results suggest that high Mn content promotes, on the one hand, appealing morphological properties, such us high surface area and pore volume, and, on the other hand, the coexistence of two structural phases (mixed oxide phase and segregated manganese oxide), whose synergy provides high variability of Mn species with different oxidation state and oxygen mobility.

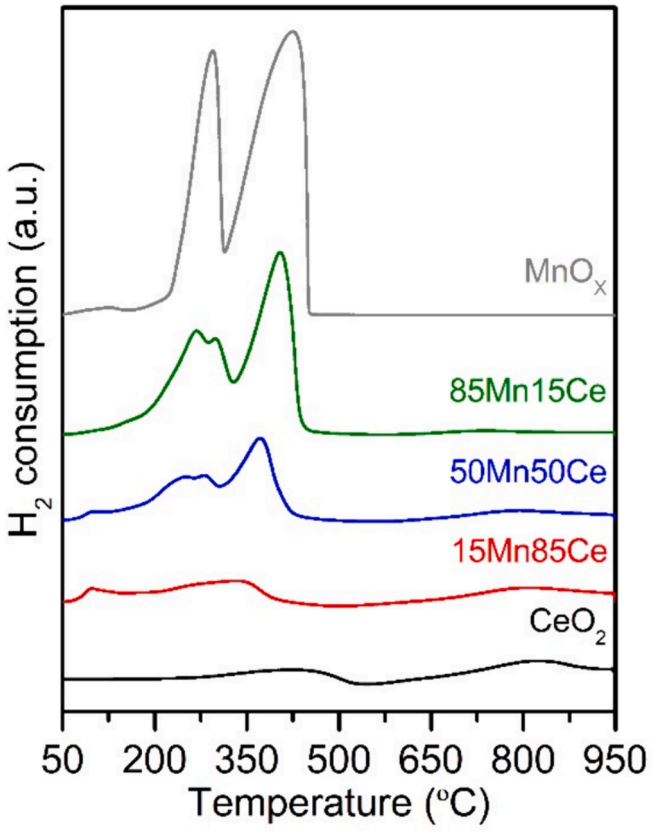

Fig. 6. H_2-TPR profiles of MnO_X-CeO_2 samples (20 mg) heated at 10 °C/min in a continuous flow of 5 % H_2/Ar (50 cm^3/min). Samples were pre-treated at 500 °C for 45 min with a continuous flow of 5 % O_2/He (50 cm^3/min).

3.2. Catalytic oxidation of o-DCB

3.2.1. Activity test

Fig. 7 shows the o-DCB conversion profiles of the samples with different Mn and Ce contents. All of them exhibit a regular sigmoid S-shape, composed by two steps in which the conversion increases with temperature. Between these two steps, there is a small drop in the conversion. In the first step conversion increases with temperature above 100 °C up to a maximum between 200 and 250 °C, depending of the catalyst sample. The second step occurs above 260 (85Mn15Ce) by

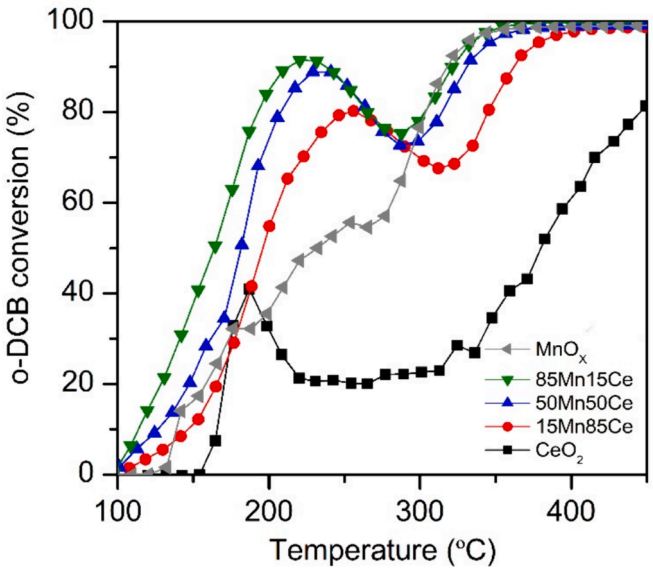

Fig. 7. o-DCB conversion over MnO_X-CeO_2 samples, prepared by co-precipitation and submitted to a flow of $2L_N$/min composed of o-DCB (100 ppm), O_2 (10 %) and Ar to balance, at 1.5 atm, and a temperature rate of 1.5 °C/min.

conversion increase up to near total conversion. This particular shape of the light-off curves have been attributed in the literature to self-inhibition effect, competitive adsorption of other compounds in the mixture, or partial deactivation of some active sites [36–38]. Further experiments in steady condition were made to assess this particular behaviour in transient conditions, which are discussed below in section 3.2.2.

Pure manganese oxide has a higher catalytic activity than pure cerium oxide over the whole temperature range. Similarly, in the bimetallic samples, the increase in Mn content shifts the o-DCB conversion profiles towards lower temperatures. These results point out that Mn is the most active metal in o-DCB oxidation.

However, Ce also plays an important role on catalytic activity, since bimetallic 50Mn50Ce and 85Mn15Ce catalysts lead to higher o-DCB conversions than pure manganese oxide, despite their lower Mn contents. This fact means that the enhancement in oxygen mobility and storage provided by Mn incorporation into CeO_2 structure improves the oxidative capability and, consequently, o-DCB oxidation can occur at lower temperatures.

The most active sample was 85Mn15Ce sample in the whole range of temperature, which leads to total conversion of o-DCB around 330 °C. These results show that the MnO_X-CeO_2 catalysts tested here have significantly better activity compared to the catalysts based on vanadium and zeolites the authors have been reported formerly under the same conditions [2,22,23,39].

The excellent catalytic activity of 85Mn15Ce sample cannot be related only to the improvement of the catalytic properties arising from the incorporation of Mn into CeO_2 structure, because XRD results corroborated this catalyst is also composed of another segregated manganese oxide phase, resulting from the saturation of mixed oxide phase at such Mn content. A similar result was reported by Ye and co-workers [40], who established that the limit of Mn/(Mn + Ce) ratio allowing Mn incorporation into CeO_2 structure is between 0.6 and 0.75. On this basis, the synergy between the two phases composing the catalyst, that is mixed oxide phase with high interaction between Mn and Ce and segregated manganese oxide phase, will favour the high catalytic activity in o-DCB oxidation.

3.2.2. *Stability tests*

In CVOCs oxidations, catalyst stability is an important feature to consider because these types of reactions are reported to cause a catalyst deactivation [41,42]. Inhibition of the active sites can not only affect the reaction rate, but also can change the reaction pathway, resulting in a loss of activity and/or selectivity towards the desired products. Catalyst deactivation of the most active catalyst, 85Mn15Ce, was assessed by TOS experiments at two different temperatures. The two selected temperatures were 200 and 300 °C, in order to consider the stability at each of the steps where o-DCB conversion increased with temperature (Fig. 7). The feeding stream for TOS experiments was the same as the one used in the light-off experiments, in which catalytic activity of samples with different Mn and Ce content was evaluated.

Fig. 8 shows the results of TOS experiments. At 200 °C, o-DCB conversion strongly decreases from 95 % (at the first few minutes of operation) to almost zero after three hours as a consequence of an important catalyst deactivation. The main product of oxidation reaction is CO_2, although its concentration decreases over time as o-DCB conversion drops. CO is hardly produced, and no chlorinated organic by-products were detected. According to literature, this deactivation of MnO_X-CeO_2 formulation in the oxidation of chlorinated compounds is mainly associated to Cl adsorption at the catalyst surface [3,41,43].

At 300 °C, o-DCB conversion is rather stable within the first hour of operation. Then, conversion decreases steadily down to 65 %, but it stabilizes after 18 h of operation, and does not deactivate further This value is very similar to the one obtained in the light-off experiments (Fig. 7). According to Fig. 8B, CO_2 is the main product of oxidation reaction, although there is some production of CO and chlorinated organic

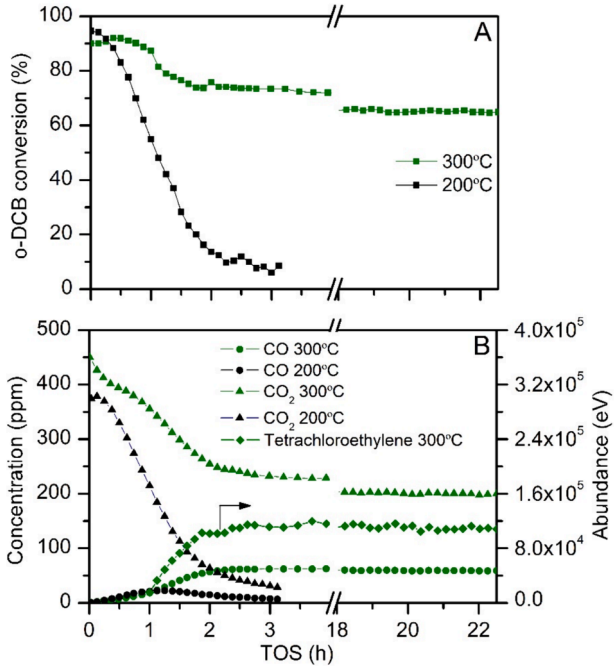

Fig. 8. Time on stream (TOS) experiment for o-DCB oxidation over 85Mn15C at a constant temperature (200 or 300 °C), flow (2L_N/min), composition (2L_N/min, 100 ppm o-DCB, 10 % O_2 and Ar to balance) and pressure (1.5 atm). A) o-DCB conversion profiles and B) CO, CO2 and tetrachloroethylene production.

by products. Chlorinated organic compounds, identified by GC–MS, were tetrachloromethane, tetrachloroethylene and trichlorobenzene. Fig. 8B only shows the tetrachloroethylene signal trend, as it is the most produced chlorinated organic compound. CO_2 concentration follows the same trend as o-DCB conversion, that is, decreasing at the beginning and stabilising at the end of the experiment. In contrast, CO concentration and tetrachloroethylene signals increase simultaneously with the drop in CO_2, and they stabilise at the end of the experiment.

The trends followed by oxidation products at 300 °C show a loss in the oxidative capability of the catalyst as the experiment proceeds, which negatively affects the total oxidation of o-DCB. This fact is particularly remarkable because it was not observed at 200 °C (only CO_2 was produced) despite the decrease in o-DCB conversion caused by catalyst deactivation.

On the other hand, thermodynamics proves the possibility of formation of chlorinated species different to HCl in the operating studied conditions, such as Cl_2, from the Deacon reaction ($4HCl + O_2 \leftrightarrow 2Cl_2 + 2H_2O$), and even ClO_2 and chloramines. However, Cl_2 has not been detected, which means that Deacon reaction and ClO_2 formation does not take place, probably because reaction conditions are kinetically unfavourable. HCl is the only inorganic chlorinated compound detected under o-DCB oxidation. That is why selectivity HCl/Cl_2 it is not shown in Fig. 8.

The different o-DCB oxidation in terms of both conversion and products formation, as a function of temperature, is proposed to be related to the presence of active sites with different oxidative capability. This was confirmed with an additional light-off experiment over 85Mn15Ce catalyst, in which the temperature was increased by steps and was kept constant in each step until conversion was stabilized down to experimental error (Fig. 1). Fig. 9 shows the comparison between the two lights-offs measured by steady heating ramp of 1.5 °C/min (Ramp) and measured by temperature increase by steps (Step). The new light-off is significantly different below 270 °C with a standard shape of only one step, with a light-off section around 265 °C and conversion lower than 10 % below 225 °C. Then, results shown in Figs. 7 and 8 confirm that MnO_X-CeO_2 catalysts are composed of two type of active sites, some with

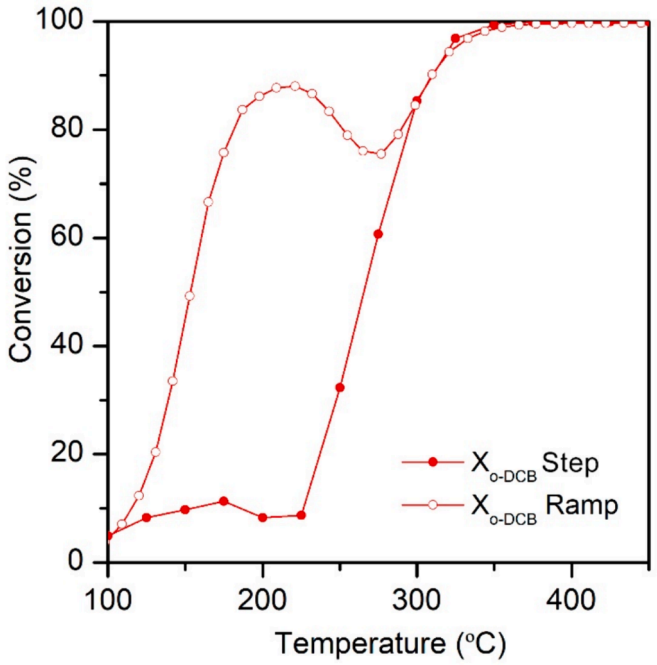

Fig. 9. Comparison between light-off experiments measured by steady heating ramp of 1.5 °C/min (Ramp) and measured by temperature increase by steps (Step). Catalyst sample 85Mn15Ce, prepared by co-precipitation and submitted to a flow of $2L_N$/min composed of o-DCB (100 ppm), O_2 (10 %) and Ar to balance, at 1.5 atm.

high oxidative capacity, very active at low temperatures, but easily deactivated, and others with low oxidative capacity resistant to deactivation. This also explains the particular shape of conversion profiles obtained in the evaluation of the catalytic activity as a function of Mn content (Fig. 7). Thus, in bimetallic catalysts, the increase in o-DCB conversion at low temperature (first step) is promoted by the active sites with higher oxidative capability. After that, the drop in o-DCB conversion is caused by the progressive deactivation of these active sites. Finally, the activation of the active sites with lower oxidative capability with the further increase in temperature leads to increase the o-DCB conversion again (second step).

According to characterization results, H_2-TPR technique concluded that Mn incorporated into CeO_2 structure (mixed oxide phase) is more susceptible to be reduced than Mn segregated as oxide, due to the better oxygen mobility resulting from the higher interaction degree between Mn and Ce. Indeed, the promotion of oxygen mobility favours oxidative capability and active sites with higher oxidative capability would be mostly promoted by mixed oxide phase. On this basis, the active sites with higher oxidative capability mainly contribute to the catalytic activity at low temperatures, leading to total oxidation of o-DCB. However, they are strongly deactivated, causing the drop in o-DCB conversion observed in TOS experiment at 200 °C. At higher temperatures, other active sites, associated to segregated as Mn_2O_3, with lower oxidative capability and more resistant to deactivation become active enough to perform o-DCB oxidation. As a consequence, CO and chlorinated organic compounds are produced, which is in agreement with TOS experiment at 300 °C. The contribution of these active sites with lower oxidative capability is low at the beginning of the operation, but it increases as the active sites with higher oxidative capability are deactivated. This is deduced from the drop in o-DCB conversion and the only production of CO_2 at the beginning of TOS experiment at 300 °C.

The 85Mn15Ce samples used in the TOS experiments at 200 and 300 ° C (Fig. 7) were characterized by TG/MS, SEM-EDX, XRD, N_2-fisisorption, and H_2-TPR in order to get an image of what might be the cause of deactivation, especially of the active centres with high oxidative capacity. dTG profiles exhibit two peaks around 225 and 485 °C. The larger area under the dTG profile of the used catalyst from TOS experiment at 200 °C denotes the removal of a larger amount of deactivating species (around 4 %), in comparison to the catalyst from TOS experiment at 300 °C (around 2 %). The obtained $m/z = 44$ (CO_2) profiles matched well with dTG profiles, evidencing that deactivating matter is composed by carbon-based compounds. However, no m/z associated to chlorine was detected. However, the EDX revealed the presence of a remarkable amount of surface chlorine in both samples as shown as in Table 2. Carbon composition was also estimated by EDX, in a similar proportions by TG.

Table 2 also shows the crystal size of the two main phases (fluorite and Mn_2O_3) obtained from XRD and, the specific surface area, mean pore volume and mean pore diameter obtained from N_2-physisoprtion. The crystal size of both, fluorite and Mn_2O_3 phases, increases in the used catalysts, which denotes a phase segregation, and thus, a negative effect on the oxygen mobility, due to the lower interaction degree between Mn and Ce. This fact could be related to a sintering crystal phases, promoted by the deposition of non-removable deactivating matter. The lower interaction between Mn and Ce in the used 85Mn15Ce catalysts contributes to the loss of structural defects, which decreases the specific surface area and makes higher the pore size in comparison to the fresh 85Mn15Ce catalyst. In addition, the deposition of deactivating matter also contributes to deteriorate the morphology of the catalyst through the blocking of pores, as it is denoted by the slightly decrease in the pore volume in the used samples.

Fig. 10 shows the TPR profiles of fresh and used catalysts in TOS experiments. The shift of reduction profile of used catalysts towards high temperature in comparison to fresh catalyst denotes a decrease in redox properties. The loss of reducibility is clearly associated to phase segregation evidenced by XRD, which reduces oxygen mobility. Moreover, there is a remarkable difference in the H_2 consumption associated to Mn in high oxidation state (H_2 uptake at low temperature), because it is composed by two well-differentiated subpeaks (at 270 and 300 °C) in the fresh sample, whereas it is composed by a tiny peak and a shoulder strongly overlapped with the H_2 uptake at high temperature in the used samples. On the other hand, Fig. 10 also reports a higher H_2 consumption in the used 85Mn15Ce catalysts, which could be associated to an additional H_2 consumption of deactivating matter. This explanation is in accordance with the slight higher H_2 consumption of used catalyst in TOS experiment at 200 °C in comparison to that of used catalyst in TOS experiment at 300 °C, because of the higher amount of deactivating species observed by TG and EDX. Therefore, the noticeable difference in the H_2 consumption at low temperature between fresh and used samples suggests that deactivating matter affects Mn in high oxidation state, either Mn^{4+} (in high interaction with Ce) or Mn^{3+} (in Mn_2O_3 oxide). As concluded in section 3.1, the co-existence of these two Mn species is essential to provide an effective oxygen mobility, so their deficit affects the reducibility of the sample, which leads to a reduction of used catalysts at higher temperatures than the fresh catalyst. Furthermore, the H_2-TPR results agree with those obtained in TOS experiment, where it was evidenced the influence of catalytic deactivation in the o-DCB oxidation at low temperature. In this sense, at low temperature, oxygen mobility is a key factor for the activity of surface oxygen. Thus, the negative effects of deactivating species in the metal species that provides an effective oxygen mobility [44], is the cause that leads the decrease of o-DCB conversion at low temperature.

3.2.3. *In-situ FTIR experiments of o-DCB adsorption*

In-situ FTIR spectra of surface species resulting from o-DCB adsorption over the 85Mn15Ce sample, at 100 and 250 °C, are shown in Fig. 11. Resulting spectra are quite complex, and the assignment of the main IR bands is summarized in Table 3.

The adsorption of o-DCB at 100 °C, Fig. 11A, leads to the appearance of several sharp bands at 1570, 1455 and 1435 cm^{-1} related to the stretching modes (8a, 19a and 19b, respectively) of the aromatic ring

Table 2
Surface Cl and C composition from EDX analysis and structural and textural properties of used 85Mn15Ce catalysts in TOS experiments.

Catalyst	Cl content (%wt)	C content (%wt)	Fluorite crystal size (nm)	Mn_2O_3 crystal size (nm)	S_{BET} (m^2/g)	V_P (cm^3/g)	d_P (nm)
85Mn15Ce (200)	1.9	5.9	6	25	58	0.23	13.3
85Mn15Ce (300)	1.7	4.9	6	27	41	0.24	19.6
85Mn15Ce	0.1	–	4	17	87	0.25	9.0

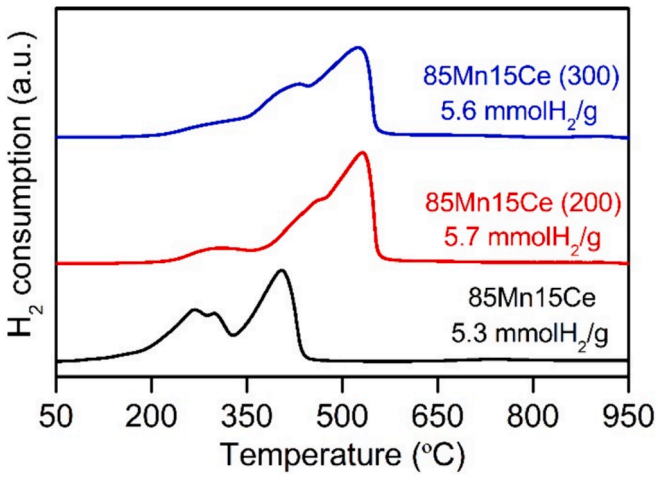

Fig. 10. TPR profiles of used 85Mn15Ce catalysts in TOS experiment and fresh 85Mn15Ce catalysts.

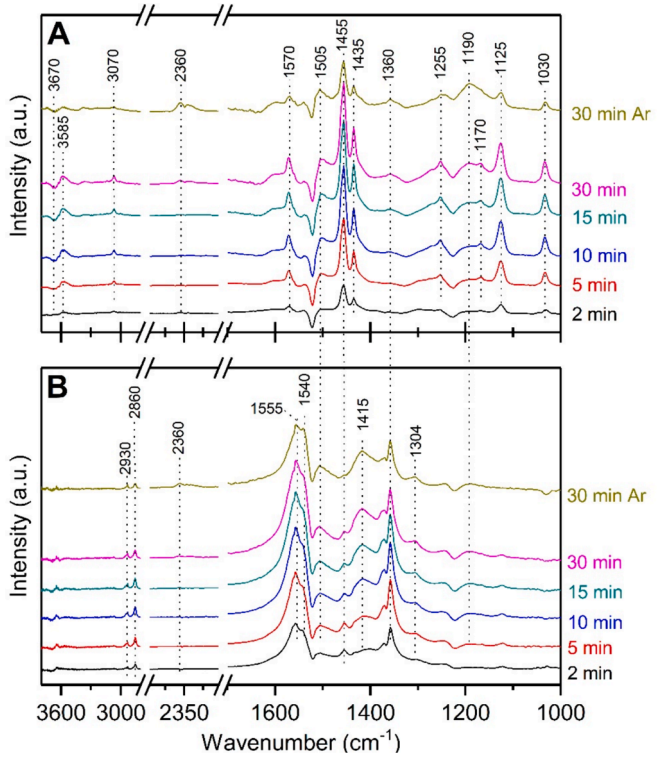

Fig. 11. FTIR spectra after exposing the 85Mn15Ce catalyst to 1000 ppm o-DCB/Ar and followed by a purge with Ar at A) 100 °C and B) 250 °C.

[43,45–48]. In addition, the band at 1255 cm^{-1} evidences C—H bonds of aromatic ring [49,50], whereas the bands at 1170, 1125, and 1030 cm^{-1} are associated to C—Cl stretching [45,46]. Additionally, the weak band at 3070 cm^{-1} is due to stretching of aromatic C—H bonds [45].

Table 3
Assignment of the IR bands identified in the adsorption of o-DCB.

Band (cm^{-1})	Assignment	Reference
1570, 1455, 1423	Aromatic stretching	[48,50]
1255	C—H in plane bending	[48,50]]
1170, 1125, 1030	C—Cl stretching	[48,50]
1190	Phenate (C—O stretching)	[48,50]
1505	Maleate (C—O stretching)	[48,50]
1540, 1360	Formate (C—O stretching)	[48,50,52]
1555, 1415	Acetate (C—O stretching)	[47,55,56]
1370	CH_2 stretching	[56]
1304	Enolic	[51,57]
1610	Hydroxyl	[52]
2350	CO_2 gas	[52,54]
2930, 2860	C—H stretching	[55,58]
3070	Aromatic C—H stretching	[45]

Increasing the exposure time favours a gain in the intensity of the bands above described and leads to the appearance of other bands related to intermediate species resulting from the reaction between adsorbed o-DCB and surface oxygen of the catalyst. In detail: the band at 1190 cm^{-1} is associated to C—O vibrational mode of phenate species [45], which is considered as the first intermediated species in o-DCB oxidation. On the other hand, the bands at 1505 and 1360 cm^{-1} have been previously assigned to COO— stretching modes of maleate [47,50] and formate [51,52] species, respectively. In the high wavenumber region, there is a negative band at 3670 cm^{-1} along with a broad band with maximum around 3585 cm^{-1}. This result suggests the disappearance of surface hydroxyl groups as a consequence of their interaction with o-DCB both through H-bonds and through o-DCB chemisorption [53], as discussed in the following.

The presence of typical bands of molecularly adsorbed o-DCB suggests that, at 100 °C o-DCB is hardly oxidised on the catalytic surface due to the low activity of oxygen species. o-DCB adsorption can occur through the coordination of chlorine atoms with exposed metal ions acting as a Lewis acid site, or through the interaction with a surface hydroxyl group by means of the formation of weak H-bonds. The electron-rich benzene ring can also be involved in this first-step interaction. To ascertain this point, in another set of experiments, DCB has been adsorbed at the catalyst surface at room temperature and upon heating in static conditions. In the 1700–2000 cm^{-1} frequency region (Fig. S1), weak bands due to combination and overtones of the aromatic ring are detected at 1918, 1950, 1795 cm^{-1}, that is, very close to those reported for pure liquid o-DCB, and stable also following prolonged outgassing. These findings have been previously explained by considering the aromatic ring adsorption at the surface to be perpendicular, thus o-DCB interacts mainly through its Cl substituents with the catalyst surface [46].

On the other side, the detection of adsorbed oxygenated fragments such as carboxylate species suggests that a fraction of o-DBC already undergoes deep oxidation, in spite of the low reaction temperature. This is confirmed by the appearance of a roto-vibrational band contour between 2360 and 2340 cm^{-1} after 30 min of exposure time. These features are related to CO_2 in the gas phase [52,54] and show that at least part of adsorbed o-DCB is completely oxidized.

The intensity of the bands associated to molecularly adsorbed o-DCB decreases after purging with Ar. Conversely, the intensity of bands associated to phenate species and CO_2 increases, which looks rather

unusual since it could be expected that their intensity should remain stable or decrease slightly. But it is also possible that the adsorbed o-DCB or part of it is still reacting with surface oxygen during the purge time, thus increasing the amount of reaction intermediates adsorbed on the catalyst. It is probable that at low temperature, as the opening of the aromatic ring is difficult, so that after the adsorption period prior to purging with Ar, the surface oxygen has not been completely consumed. Hence, it can react with the adsorbed o-DCB or part of it giving reaction intermediates even in the purging stage. This result confirms the chemisorption of o-DCB through Cl substitution by surface oxygen, leading to strongly adsorbed species, the likely intermediates of o-DCB total oxidation.

On the other hand, Fig. 11B shows the resulting spectra after o-DCB adsorption at 250 °C. The spectra are completely different to those obtained at lower temperature. The bands at 1555 and 1415 cm^{-1} (COO— asymmetric and symmetric stretching mode) denote the presence of acetate species [47,55,56], and those at 1540 and 1360 cm^{-1} (COO— asymmetric and symmetric stretching mode) are associated to formate species [49,50,52]. The bands ascribed to phenate (1190 cm^{-1}) and maleate (1505 cm^{-1}) species, which were the main oxygen-containing species at 100 °C, are also present at 250 °C but their intensities are lowered. Another band at 1304 cm^{-1} has been assigned to enolic species [51,57]. The presence of enolic species, together with adsorbed acetates, could also be supported by the new bands at 2930 and 2860 cm^{-1}, which are related in the literature to different types of C—H stretching [55,58].

In the high wavenumber region, there is a lesser contribution of o-DCB H-bonded to surface hydroxyl groups, as denoted residual weak negative bands near 3660 cm^{-1}. The absence of broad a band around 3585 cm^{-1} also evidences this. This result could be associated to the interaction between a larger amount of chlorides generated in the reaction and hydroxyl groups, leading to the removal of Cl adsorbed as HCl; a similar hypothesis has been already proposed by Gao et al. [53] after studying o-DCB adsorption over Fe-based catalysts.

On this basis, the absence of the bands due to molecularly adsorbed o-DCB (bands of aromatic ring and C—Cl bonds) suggests that, at 250 °C, o-DCB is adsorbed and, then, rapidly oxidized by lattice oxygen leading to the intermediate species mentioned above. Actually, the band associated to stretching of aromatic C—H (3070 cm^{-1}) does not appear anymore in the spectra. However, the further total oxidation of the intermediate species is not fast, since the bands of CO_2 in the gas phase do not appear until 30 min of exposure time. This could be related to the absence of oxygen in the gas phase.

In order to assess the impact of the presence of oxygen on the species formed during o-DCB oxidation, co-adsorption of o-DCB and O_2 was carried out at 100 and 250 °C. The resulting spectra are shown in Fig. 12 and Table 3 summarizes the assignment of the obtained bands.

The adsorption of o-DCB in the presence of oxygen at 100 °C, Fig. 12A, leads to similar spectra than those obtained in the absence of oxygen. There are bands associated to C—C bonds in the aromatic ring (1570, 1455 and 1435 cm^{-1}), C—Cl bonds (1170, 1125 and 1030 cm^{-1}) and C—H bonds (1255 and 3070 cm^{-1}) of adsorbed o-DCB. In addition, the bands of maleate, formate and phenate intermediate species are present in the spectra at 1505, 1360 and 1190 cm^{-1}, respectively. These bands of intermediate species appear just after exposing the feeding stream to the catalyst, whereas in the absence of oxygen (Fig. 11A) they appeared later, after 30 min of exposure time. Thus, the presence of oxygen in the gas phase favours a faster oxidation of o-DCB.

On the other hand, the main bands obtained in the adsorption of o-DCB in the presence of oxygen at 250 °C, Fig. 12B, are associated to —COO— stretching modes of acetate (1555 and 1415 cm^{-1}) and formate (1540 and 1360 cm^{-1}) species. Additionally, two broad shoulders appear between 1650 and 1500 cm^{-1}. The one located at 1505 cm^{-1} is likely due to asymmetric stretching mode of maleate species (whose corresponding symmetric mode could be masked by stronger absorptions), whereas the other located at 1610 cm^{-1} has been assigned to the bending vibration of hydroxyl groups of water produced in the oxidation

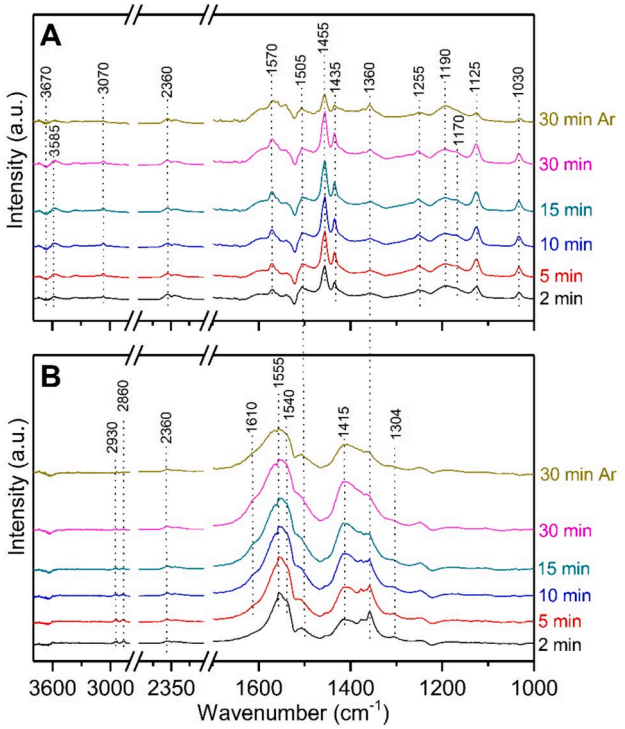

Fig. 12. FTIR spectra after exposing the 85Mn15Ce catalyst to 1000 ppm o-DCB+5% O2/Ar and followed by a purge with Ar at A) 100 °C and B) 250 °C.

of o-DCB [59]. The small band at 1304 cm^{-1} also evidences the presence of enolic species. Moreover, the presence of C—H bonds in the different intermediate species identified at 250 °C is evidenced by the bands at 2930, 2860 and 1255 cm^{-1}.

Comparison between the obtained results points out a notable difference in the distribution of intermediate species as a function of temperature. At 100 °C, o-DCB coordination and reactive adsorption occurs, leading to the formation of phenate species. The predominance of phenate and maleate species indicates the low activity of the catalyst in the breaking of the aromatic ring at such low temperature. Acetate, enolic and formate species were the most important at 250 °C, characterized by a complex pattern of carboxylate bands in the 1600–1200 cm^{-1} region and by different types of C—H stretching modes in the 2930–2860 cm^{-1} region, that do not appear in the spectra at 100 °C. Thus, increasing temperature favours the ring-breaking to give small adsorbed oxidized fragments. The appearance of CO_2 in the gas phase (bands at 2360 and 2340 cm^{-1}) at 100 °C and 250 °C suggests that a small amount of adsorbed o-DCB is completely oxidized too.

3.2.4. Reaction pathway

In-situ FTIR results shows that the reaction between adsorbed o-DCB and lattice oxygen of the catalyst results in the formation of oxidized intermediate species also in the absence of oxygen in the gas phase.

Scheme 1 summarizes the main steps that compose the reaction pathway, which has been proposed on the basis of the intermediate species identified by in-situ FTIR. o-DCB oxidation starts with a chlorine abstraction of at least one of the chlorine atoms of o-DCB by a nucleophilic substitution, leading to the formation of phenate species (A). FTIR results also suggest that o-DCB can interact with surface hydroxyl groups, mainly at low temperature.

Phenate species can undergo a further chlorine abstraction by a nucleophilic substitution, in which the second chlorine atom of o-DCB is substituted by an oxygen belonging to a close active site, likely leading to the formation of catecholate and benzoquinone-type species as reported in the literature (B) [59,60]. Subsequently, the aromatic ring cleavage will occur through the reaction of catecholate and/or

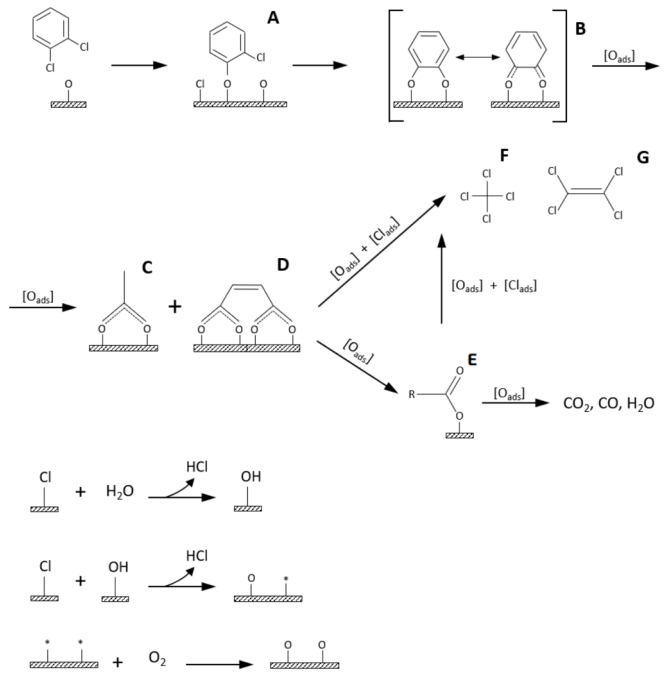

Scheme 1. Reaction pathway proposed for o-DCB oxidation over MnOX-CeO2 catalysts.

benzoquinone-type species with surface oxygen of the catalyst, producing acetate (C) and maleate species (D). Actually, in our reaction conditions no evidence of the presence of catecholate species was found by FTIR. However, this type of intermediates is widely reported to be formed as a consequence of the oxidation of phenate species, so its absence in FTIR spectra could be associated to a fast oxidation towards maleate species.

Maleate species are then oxidized to other intermediates, such as acetate, formate and enolic species (E), which are eventually oxidized towards CO, CO_2 and H_2O. However, these intermediates can react to a minor extent with adsorbed chlorine, leading to the desorption of chlorinated organic by-products (F and G). In fact, the formation of tetrachloromethane and tetrachloroethylene was already identified by GC–MS in the stability test. In this respect, it should be noted that trichlorobenzene was also identified, although in a lower amount than the other oxidation by-products, so chlorination reaction of adsorbed intermediates can also occur before the cleavage of the aromatic ring.

Finally, active sites involved in o-DCB oxidation are re-oxidized with the oxygen from the gas phase in a typical Mars-Van Krevelen mechanism. In addition, adsorbed chlorine can be also removed through the reaction with water or even with a surface hydroxyl group producing HCl. This hypothesis has been proposed based on the progressive disappearance of bands related to o-DCB H-bonded to surface hydroxyl groups as temperature increases.

The different distribution of IR bands between Fig. 11A and B and Fig. 12A and B, is related to the presence of two types of active sites: One the one hand, active sites with higher oxidising capacity, corresponding to the mixed oxide phase, due to their higher oxygen mobility, but lower resistance to deactivation. On the other hand, active sites have a lower oxidising capacity, corresponding to the segregated manganese oxide phase, which are more resistant to deactivation, as concluded in section 3.1 and section 3.2.2.

The active sites with higher oxidative capability promote faster oxidation of the intermediate species produced after aromatic ring cleavage (absence of acetate, formate and enolic species), then phenolate species oxidation should be the rate limiting step at low temperature. However, at higher temperatures, the contribution of the active centres with lower oxidative capacity becomes greater due to deactivation of sites with high oxidative capacity. Over segregated manganese oxide phase, and at high temperature, chlorine abstraction and the opening of aromatic ring is relatively faster (no phenate and maleate species were observed). Conversely, the rate of decomposition acetates, formates and enoliates is relatively lower (presence of acetate, formate and enolic intermediate species in the spectra). Additionally, their higher resistance to deactivation, means the interaction between these active sites and deactivating species (mainly Cl) may favours the chlorination of acetates, formats and enolic, which is in line with the production of chlorinated organic compounds at high temperature in the stability test. In fact, the number of carbons of these chlorinated organic compounds, mostly tetrachloroethylene and tetrachloromethane, is similar to that of acetate and formate species.

So, it is found that results in the characterization (section 3.1), in catalyst stability (section 3.2.2) and in FTIR spectra (section 3.2.3), are in line and allow to explain the differences of catalyst behaviour at low and high temperature.

3.3. Catalytic oxidation of o-DCB in the presence of selective reduction of NO by NH_3

3.3.1. Activity tests

This section addresses the effect that NO reduction has on o-DCB oxidation. For this purpose, o-DCB oxidation was carried out simultaneously with NO reduction in a light-off experiment with a feeding stream composed of o-DCB (100 ppm), O_2 (10 %), NO (300 ppm), NH_3 (300 ppm) and Ar to balance. The results (Fig. 13), conversion of o-DCB

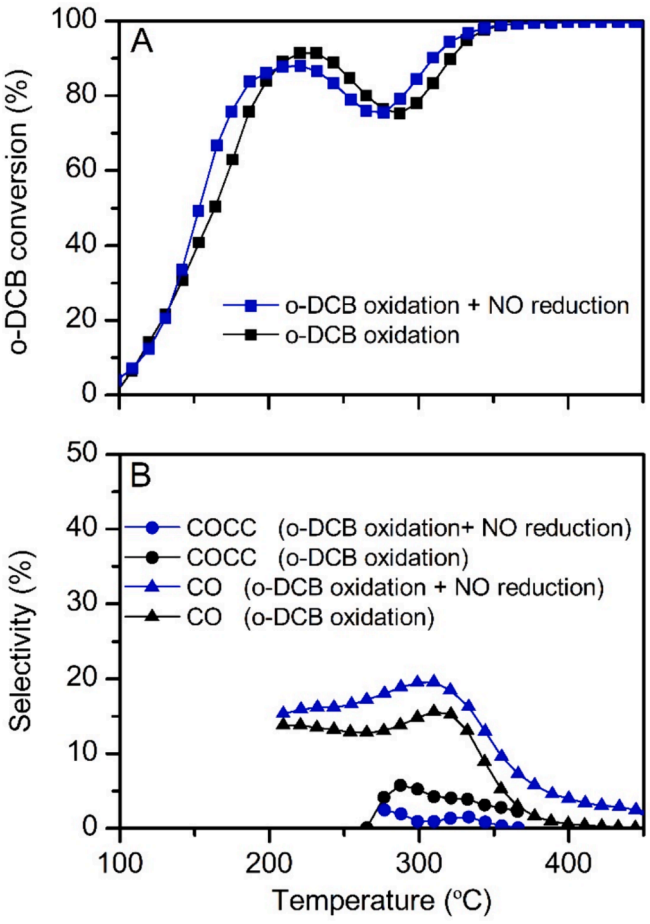

Fig. 13. Comparison of o-DCB oxidation ($2L_N$/min, 1.5 atm, 1.5 °C/min, o-DCB (100 ppm), O_2 (10 %) and Ar to balance) in the presence and the absence of NO (300 ppm) reduction over 85Mn15Ce. A) o-DCB conversion profiles and B) selectivity towards CO and chlorinated organic compounds (COCC).

and selectivity to CO and chlorinated hydrocarbons (COCC), have been compared with those obtained in section 3.2.1,

Similar conversion profiles are obtained in the presence and in the absence of NO reduction (Fig. 13A). Nonetheless, NO reduction favours oxidation reaction, since o-DCB conversion profile shifts to lower temperatures when both reactions occur simultaneously. CO_2 is the main oxidation product, whereas a small amount of CO and chlorinated organic compounds (COCC) are produced. Fig. 13B shows that NO reduction slightly increases the selectivity towards CO, i.e. from 15 % to 20 % at 300 °C, and decreases the selectivity towards chlorinated organic compounds, i.e. from 5 % to 1 % at the same temperature. In addition, the temperature range at which chlorinated organic compounds are produced narrows when o-DCB oxidation is performed simultaneously with NO reduction.

Therefore, NO reduction has a positive effect on the oxidation of both o-DCB and chlorinated organic compounds produced in the different stages of the oxidation pathway. NO reduction is also reported in the literature to enhance the oxidation of chlorinated benzenes with vanadium-based catalysts [13,61]. However, this issue leads to some conflicting results when oxidation reaction is performed with MnO_X-based catalysts, as several authors report that the presence of both NO and NH_3 has a negative effect on o-DCB oxidation [33].

In order to shed light on these aspects, o-DCB oxidation was performed over 85Mn15Ce sample separately in the presence of NO (Fig. 14) and NH_3 (Fig. 15). Several reaction runs were performed by increasing the NO concentration in the range 0 – 600 ppm while the concentration of the rest of components (o-DCB, O_2) was kept constant, as shown in Fig. 14. Another set of reaction runs were performed by increasing the NH_3 concentration in the range of 0 – 600 ppm, while the concentration of the rest of components (o-DCB, O_2) was kept constant, as shown in Fig. 15. All these tests were performed under stationary conditions at 300 °C, temperature at which the catalyst is not deactivated. Firstly, catalyst was exposed to a stream of o-DCB and oxygen for 22 h hours, until it reached steady state o-DCB conversion, as in Fig. 7. Then, NO or NH_3 was added in concentration increments, once the steady state conversion of o-DCB was reached after each increment. Fig. 14 shows that a low concentration of NO (50 ppm) increases o-DCB conversion (from 70 % to 80 %) and also favours total oxidation, since the production of CO and CO_2 increases while the production of chlorinated organic compounds (tetrachloroethylene) decreases. However, o-DCB conversion as well as oxidation products return to the same values recorded in the absence of NO with the further increase in NO concentration.

Regarding to the selectivity to chlorinated inorganics, no Cl_2, Cl_2O, chloramines were detected. Even HCl was not detected most probably due to the reaction between NH_3 and HCl or even surface chlorine to form NH_4Cl, which was detected on the particle filter located downstream the reactor [24]. It furtherly make the flormation of Cl_2 thermodinamically unfavourable.

The positive effect of NO at low concentrations is probably associated to the fact that its adsorption over the catalytic surface leads to adsorbed species with a higher oxidising power than that of oxygen, which facilitates the re-oxidation of the active sites involved in oxidation reaction. This hypothesis has been further analysed in section 3.3.2, by in-situ FTIR analysis. However, the positive effect of NO vanishes at high concentrations, because the concentration of adsorbed NO species increases to such an extent that the positive contribution arising from the re-oxidation of the active sites is balanced by the negative contribution of the competitive adsorption with o-DCB.

On the other hand, Fig. 15A shows that increasing NH_3 concentration leads to a gradual increase in o-DCB conversion from 69 %, in the absence of NH_3, to 78 %, when NH_3 concentration is 600 ppm. As for oxidation products, Fig. 15B shows a notable drop in chlorinated organic compounds (tetrachloroethylene) as NH_3 concentration increases. Simultaneously, CO and CO_2 production increase as well.

Therefore, NH_3 also has a positive effect on the selectivity of the oxidation reaction to, mainly, CO_X. The key to understand this effect lies on the behaviour followed by chlorinated organic compounds. Chlorinated organic compounds are produced by chlorination of intermediate species, thus their lower production denotes the presence of NH_3 inhibiting chlorination reactions. This inhibition is to be related to reaction between NH_3 and adsorbed Cl on the catalyst, since NH_4Cl has been obtained at the reactor outlet. The removal of adsorbed Cl releases the active sites and facilitates their re-oxidation, which promotes the slight increase in o-DCB conversion.

The positive effect that NH_3 has on o-DCB oxidation contrasts with some conclusions reported by several authors, who state that the presence of NH_3 negatively affects the oxidation of chlorinated benzenes due to the competitive adsorption for the active sites [33,62]. According to literature, NH_3 adsorption plays an important role in the reduction of NO_X over MnO_X-CeO_2 catalysts [32,63], so the adsorption of NH_3 is very likely to occur on the studied catalyst. However, the negative effect resulting from the competitive adsorption with o-DCB is not appreciable in our reaction system, because the positive effect arising from the removal of adsorbed Cl plays a dominant role.

3.3.2. *In-situ FTIR experiments on the effect of NO and NH_3 adsorbed species on o-DCB adsorption*

This section will address the effect that species resulting from NO and NH_3 adsorption have on the species produced after o-DCB adsorption. This study will allow to evaluate the involvement of NO and NH_3 in the reaction pathway of o-DCB oxidation above proposed and to complement the conclusions obtained after analysing the effect that NO and NH_3 had in the catalytic activity of o-DCB oxidation.

Fig. 16 shows the spectra obtained from o-DCB adsorption over 85Mn15Ce catalyst previously exposed to a NO-containing stream at 100 and 250 °C. At 100 °C, Fig. 16A, NO reacts at the surface giving rise to adsorbed species characterized by a broad band at 1185 cm^{-1} (NO vibrational mode) [32,64–68]. In the high wavenumber region, the negative band at 3680 cm^{-1} is associated to the consumption of surface

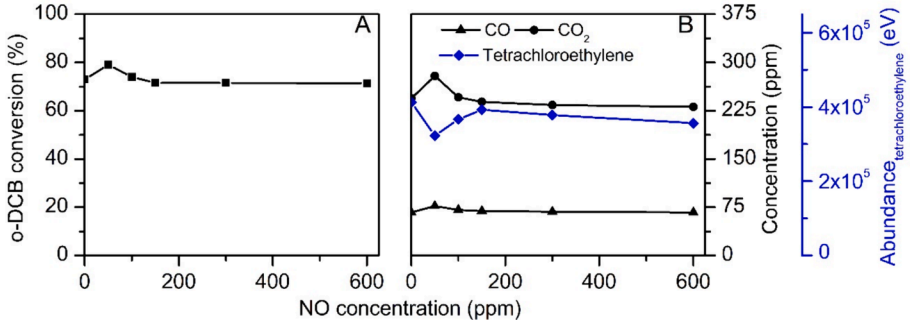

Fig. 14. Effect of NO on o-DCB oxidation over 85Mn15Ce at 300 °C ($2L_N$/min, 1.5 atm, 300 °C, o-DCB (100 ppm), O_2 (10 %) and Ar to balance). A) o-DCB conversion and B) CO, CO2 and tetrachloroethylene production.

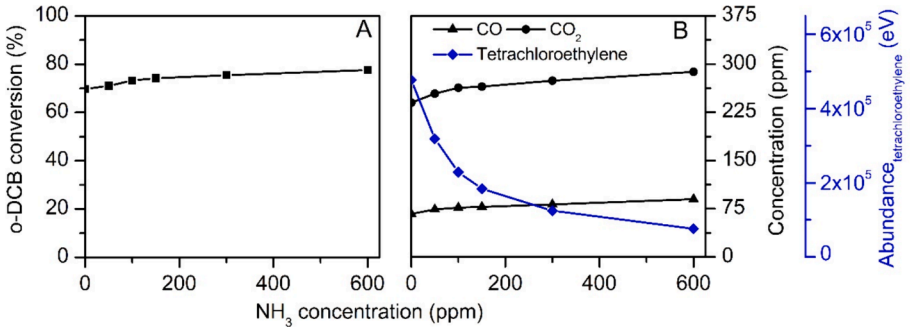

Fig. 15. Effect of NH_3 (300 ppm) on o-DCB oxidation ($2L_N$/min, 1.5 atm, 300 °C, o-DCB (100 ppm), O_2 (10 %) and Ar to balance) over 85Mn15Ce at 300 °C. A) o-DCB conversion and B) CO, CO2 and tetrachloroethylene production.

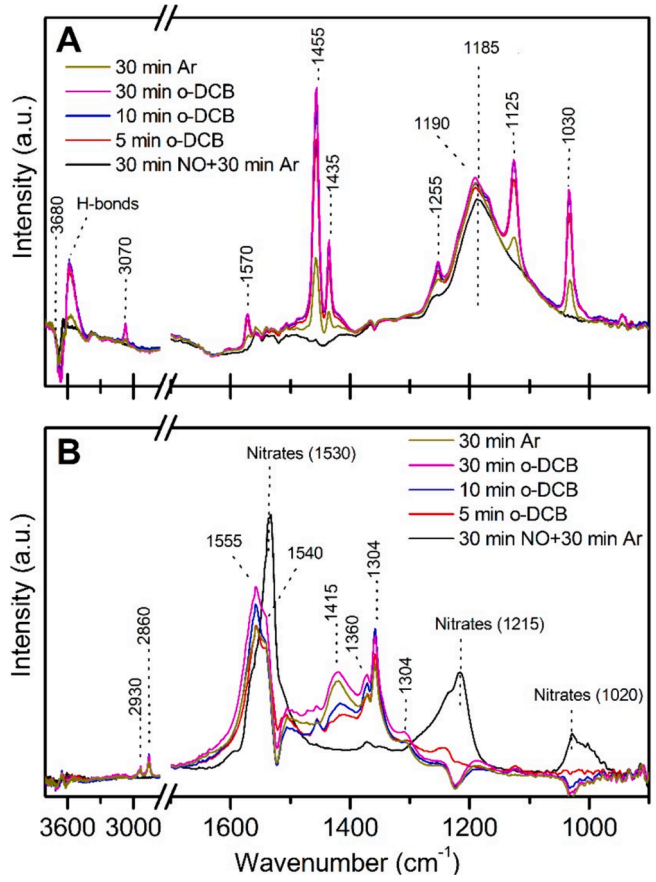

Fig. 16. FTIR spectra of 85Mn15Ce catalyst pre-treated with 1000 ppm NO/Ar and, then, exposed to 1000 ppm o-DCB/Ar followed by a purge with Ar at A) 100 °C and B) 250 °C.

hydroxyl groups as a consequence of their interaction with NO [66,69]. In parallel, it is possible to detect a broad absorption in the range 3600–3000 cm^{-1} due to H-bonds formation [66]. As discussed in the previous paragraphs, the adsorption of o-DCB leads to the appearance of additional bands related to molecularly adsorbed o-DCB, i.e., those related to the aromatic ring (1570, 1455, 1435 cm^{-1}), C—H stretching (1255 cm^{-1}) and C—Cl bonds (1125 and 1030 cm^{-1}) [66,70–72]. The intensity of the band at 1190 cm^{-1}, due to NO adsorbed species, apparently increases, likely due to the overlapping with the band related to growing phenate species, which also appears around 1190 cm^{-1} [32,73–75]. The absence of consumption of NO species after o-DCB adsorption suggests that these species are not involved in the oxidation of o-DCB [76].

At 250 °C, Fig. 16B shows a change in the resulting species from NO adsorption, since the appearance of several bands at 1530, 1215 and 1020 cm^{-1} also suggest the formation of nitrate species [77,78]. However, after o-DCB adsorption, a different behaviour is observed compared to lower temperature, since the bands associated to nitrate species progressively disappear with longer exposure times to o-DCB feeding. In fact, the absence of nitrate bands is appreciable after feeding o-DCB for 10 min. Simultaneously, o-DCB adsorption leads to the appearance of acetate (1555 and 1415 cm^{-1}), formate (1540 and 1360 cm^{-1}) and enolic (2930, 2860 and 1304 cm^{-1}) species. The disappearance of nitrate bands denotes the involvement of NO adsorbed species as surface nitrates in o-DCB oxidation. Similar intermediate species have been identified by comparing in-situ FTIR results obtained after o-DCB adsorption in the absence (Fig. 12B) and presence (Fig. 16B) of NO. This fact suggests that nitrate species do not alter the reaction pathway previously proposed for o-DCB oxidation and, thus, their involvement is probably related to a promotion of the re-oxidation of the active sites. This re-oxidation of the active sites is faster than that carried out by oxygen from the gas phase, explaining the positive effect that low concentrations of NO had on o-DCB oxidation (Fig. 13) [61,79,80].

Fig. 17 shows the spectra obtained from o-DCB adsorption over 85Mn15Ce catalyst previously exposed to a NH_3-containing stream at 100 and 250 °C. At 100 °C (Fig. 17A), the strong band at 1175 cm^{-1} denote NH_3 coordinated on Lewis acid sites. In the high wavenumber region, the bands at 3360, 3225 and 3130 cm^{-1} are related to NH stretching vibration. The negative band at 3660 cm^{-1} is assigned to the consumption of surface hydroxyl groups due to the formation of H-bonds with adsorbed ammonia. The molecular adsorption of o-DCB, revealed by the same bands discussed above, does not alter the bands associated to NH_3-adsorbed species.

The presence of adsorbed NH_3 species at 250 °C (Fig. 17B) is also evidenced by the band at 1175 cm^{-1}. Moreover, the low intensity of the bands located in the high wavenumber range 3360–3100 cm^{-1} suggests a notable proton abstraction of adsorbed NH_3 at this temperature. o-DCB adsorption leads to typical bands related to intermediate species of o-DCB oxidation (1415, 1360 and 1304 cm^{-1}), although the most characteristic bands of formate and acetate species around 1555 and 1140 cm^{-1} are perturbed by the broad negative bands, which seem to be associated to NH_3 adsorption at high temperature as they were not observed at lower temperature. The appearance of bands related to o-DCB adsorbed species increases the intensity of the only band related to adsorbed NH_3 (1175 cm^{-1}). However, the intensity of this band return to its previous value before o-DCB adsorption after the purge with Ar, which evidences that NH_3 keeps adsorbed after o-DCB adsorption.

The fact that the bands associated to adsorbed NH_3 species are still detected in the spectra after o-DCB adsorption at both 100 and 250 °C denotes that, probably, NH_3 adsorbed species are not involved in o-DCB oxidation and do not modify the oxidation pathway of o-DCB above proposed. Moreover, o-DCB is not such a strong base as to be able to replace ammonia coordinated over acidic sites. However, the results of

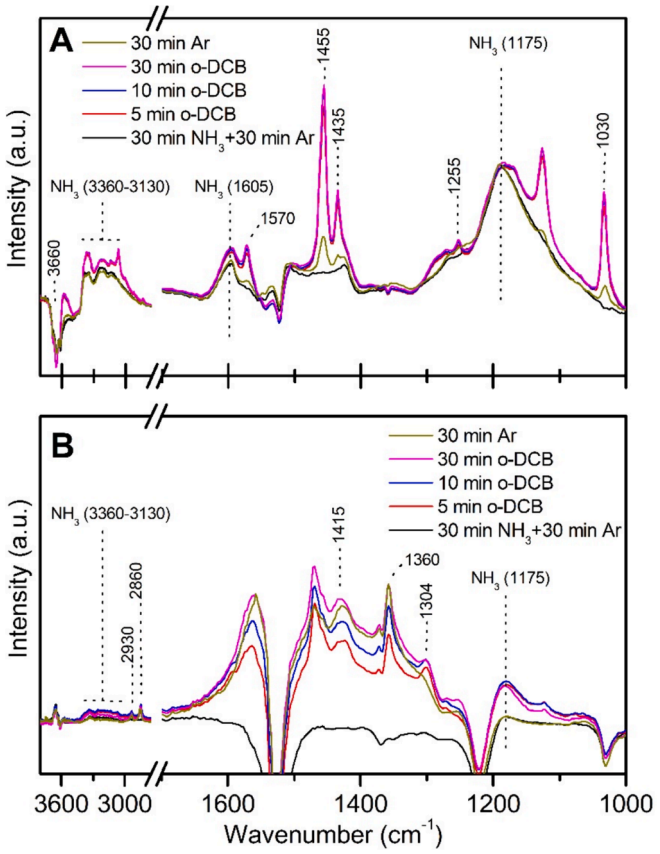

Fig. 17. FTIR spectra of 85Mn15Ce catalyst pre-treated with 1000 ppm NH_3/Ar and, then, exposed to 1000 ppm o-DCB/Ar followed by a purge with Ar at A) 100 °C and B) 250 °C.

catalytic activity indicate that the presence of NH_3 has a positive effect on o-DCB oxidation (Fig. 15). At high temperature, NH_3 is able to remove Cl from segregated manganese oxide phase, which oxidising capacity is lower, preventing from catalyst deactivation and from highly chlorinated hydrocarbons formation. However, at low temperature, NH_3 is not able to remove strongly adsorbed Cl from mixed oxide phase, leading to a rapid deactivation, even though these centres have a high oxidation capacity.

4. Conclusions

In this work, o-DCB oxidation has been studied with MnO_X-CeO_2 catalytic formulation. Mn and Ce content plays an important role in the catalytic activity, since high Mn contents favour o-DCB oxidation at lower temperatures. The better activity of the catalyst with high Mn content is associated to, on the one hand, the promotion of morphological properties (higher surface area and pore volume), and, on the other hand, the coexistence of two structural phases (mixed oxide phase and segregated manganese oxide) whose synergy provides high variability of Mn species with different oxidation state and oxygen mobility.

TOS experiments for the assessment of the catalyst stability allowed to elucidate two important features of o-DCB oxidation with MnO_X-CeO_2 catalytic formulation. First, the catalyst is deactivated in the low temperature range (below 300 °C). Second, there is a transient change in oxidative capability of the catalyst at high temperature. Both features have been proposed to be related to the presence of active sites with higher and lower oxidative capability. In this way, the active sites with higher oxidative capability greatly contribute at low temperature to o-DCB oxidation, but they are strongly deactivated. Conversely, active sites with lower oxidative capacity are resistant to deactivation but need high temperatures to actively contribute to the oxidation of o-DCB. The variability in the oxidative capability of active sites has been proposed to be associated to the presence of the different phases composing the catalyst and the different interaction between Mn and Ce that they promote.

The analysis of reaction pathway by means of in-situ FTIR points out that o-DCB oxidation follows a Mars-Van Krevelen type pathway. The first step of the proposed reaction mechanism is a nucleophilic substitution that leads to phenate species. Subsequently, a second nucleophilic substitution and the cleavage of aromatic ring generates maleate species. Maleate species are further oxidised to formate, acetate and enolic species, which are eventually oxidised to CO, CO_2, H_2O and HCl. Nonetheless, they can also react to a lower extent with adsorbed chlorine leading to chlorinated organic compounds.

The presence of active sites with different oxidative capability does not modify the proposed reaction pathway, although it favours some steps to occur faster than others, which modifies the distribution of intermediate species. Thus, the oxidation of intermediate species produced after the aromatic ring is broken is slower in the active sites with lower oxidative capability. This fact favours the chlorination of intermediate species in the operational conditions where these active sites with lower oxidative capability greatly contribute to o-DCB oxidation.

Performing o-DCB oxidation and NO reduction simultaneously favours the shift of o-DCB conversion profile to lower temperatures. Moreover, it decreases the production of chlorinated organic compounds. The presence of NO results in its adsorption through nitrate species at high temperature, which contributes to a faster re-oxidation of the active sites. Also, at high temperature, the presence of NH_3 promotes Cl removal from segregated manganese oxide phase, which oxidising capacity is lower, preventing from catalyst deactivation and from highly chlorinated hydrocarbons formation.

According to the results obtained in this work, further research is needed on reaction kinetics modelling consistent with the reaction mechanism proposed in this work, and to determine to what extent the conclusions obtained for the oxidation of o-DCB are valid for the oxidation of real PCDDs.

CRediT authorship contribution statement

J.A. Martín-Martín: Writing – original draft, Methodology, Investigation, Conceptualization. **A. Aranzabal:** Writing – review & editing, Supervision, Project administration, Funding acquisition. **M.P. González-Marcos:** Writing – review & editing, Resources, Funding acquisition, Formal analysis, Conceptualization. **E. Finocchio:** Writing – review & editing. **J.R. González-Velasco:** Writing – review & editing, Resources, Funding acquisition.

Declaration of competing interest

The authors declare that they have no known competing financial interests or personal relationships that could have appeared to influence the work reported in this paper.

Data availability

Data will be made available on request.

Acknowledgments

Authors acknowledge the financial support of Spanish Ministry of Science and Innovation through Agencia Estatal de Investigación (AEI) MCIN/AEI/10.13039/501100011033 (PID2019-107503RB-I00), Basque Government (Project IT1509-2022) and The University of the Basque Country, UPV/EHU (UFI 11/39). JAMM specially thanks MINECO/FEDER (BES-2016-077849) for the PhD grant. The authors also acknowledge technical and human support provided by SGIker (UPV/

EHU Advanced Research Facilities/ERDF, EU).

Appendix A. Supplementary data

Supplementary data to this article can be found online at https://doi.org/10.1016/j.cej.2024.155570.

References

[1] E. Finocchio, G. Busca, M. Notaro, A review of catalytic processes for the destruction of PCDD and PCDF from waste gases, Appl. Catal. B Environ. 62 (2006) 12–20, https://doi.org/10.1016/j.apcatb.2005.06.010.

[2] M. Gallastegi-Villa, A. Aranzabal, M.P. González-Marcos, B. Markaide-Aiastui, J. A. González-Marcos, J.R. González-Velasco, Effect of vanadia loading on acidic and redox properties of VO_x/TiO_2 for the simultaneous abatement of PCDD/Fs and NO_x, J. Ind. Eng. Chem. 81 (2020) 440–450, https://doi.org/10.1016/j.jiec.2019.09.034.

[3] W. Xingyi, K. Qian, L. Dao, Catalytic combustion of chlorobenzene over MnO_x-CeO_2 mixed oxide catalysts, Appl. Catal. B Environ. 86 (2009) 166–175, https://doi.org/10.1016/j.apcatb.2008.08.009.

[4] X. Guo, Y. Ma, X. Lin, X. Li, Y. Xiang, A. Wu, Reduction of polychlorinated dibenzo-p-dioxins and dibenzofurans by chemical inhibition and physisorption from a municipal solid waste incineration system, Energy Fuels 34 (2020) 11237–11247, https://doi.org/10.1021/acs.energyfuels.0c01918.

[5] F. Neuwahl, G. Cusano, J. Gómez Benavides, S. Holbrook, S. Roudier, Best Available Techniques (BAT) Reference Document for Waste Incineration. EUR 29971 EN; doi: 10.2760/761437.

[6] H. Huang, Y. Xu, Q. Fenga, D.Y.C. Leung, Low temperature catalytic oxidation of volatile organic compounds: a review, Cat. Sci. Technol. 5 (2015) 2649–2669, https://doi.org/10.1039/c4cy01733a.

[7] A. Aranzabal, J.A. González-Marcos, J.L. Ayastuy, J.R. González-Velasco, Kinetics of Pd/alumina catalysed 1,2-dichloroethane gas-phase oxidation, Chem. Eng. Sci. 61 (2006) 3564–3576, https://doi.org/10.1016/j.ces.2005.12.031.

[8] B. Miranda, E. Díaz, S. Ordóñez, A. Vega, F.V. Díez, Performance of alumina-supported noble metal catalysts for the combustion of trichloroethene at dry and wet conditions, Appl. Catal. B: Environ. 64 (2006) 262–271, https://doi.org/10.1016/j.apcatb.2005.12.008.

[9] H.L. Tidahy, S. Siffert, J. Lamonier, E.A. Zhilinskaya, A. Aboukaïs, Z. Yuan, A. Vantomme, B. Su, X. Canet, G. De Weireld, M. Frère, T.B. N'Guyen, J. Giraudon, G. Leclercq, New Pd/hierarchical macro-mesoporous ZrO_2, TiO_2 and ZrO_2-TiO_2 catalysts for VOCs total oxidation, Appl. Catal. A 310 (2006) 61–69, https://doi.org/10.1016/j.apcata.2006.05.020.

[10] J. Giraudon, T.B. Nguyen, G. Leclercq, S. Siffert, J. Lamonier, A. Aboukaïs, A. Vantomme, B. Su, Chlorobenzene total oxidation over palladium supported on ZrO_2, TiO_2 nanostructured supports, Catal. Today 137 (2008) 379–384, https://doi.org/10.1016/j.cattod.2008.02.019.

[11] M. Taralunga, J. Mijoin, P. Magnoux, Catalytic destruction of 1,2-dichlorobenzene over zeolites, Catal. Commun. 7 (2006) 115–121, https://doi.org/10.1016/j.catcom.2005.09.006.

[12] S. Scirè, S. Minicò, C. Crisafulli, Pt catalysts supported on H-type zeolites for the catalytic combustion of chlorobenzene, Appl. Catal. B Environ. 45 (2003) 117–125, https://doi.org/10.1016/S0926-3373(03)00122-X.

[13] F. Bertinchamps, M. Treinen, N. Blangenois, E. Mariage, E.M. Gaigneaux, Positive effect of NO_x on the performances of VO_x/TiO_2-based catalysts in the total oxidation abatement of chlorobenzene, J. Catal. 230 (2005) 493–498, https://doi.org/10.1016/j.jcat.2005.01.009.

[14] J. Corella, J.M. Toledo, A.M. Padilla, On the selection of the catalyst among the commercial platinum-based ones for total oxidation of some chlorinated hydrocarbons, Appl. Catal. B Environ. 27 (2000) 243–256, https://doi.org/10.1016/S0926-3373(00)00154-5.

[15] D.P. Debecker, F. Bertinchamps, N. Blangenois, P. Eloy, E.M. Gaigneaux, On the impact of the choice of model VOC in the evaluation of V-based catalysts for the total oxidation of dioxins: furan vs. chlorobenzene, Appl. Catal. B Environ. 74 (2007) 223–232, https://doi.org/10.1016/j.apcatb.2007.02.016.

[16] G. Busca, M. Baldi, C. Pistarino, J.M. Gallardo Amores, V. Sanchez Escribano, E. Finocchio, G. Romezzano, F. Bregani, G.P. Toledo, Evaluation of V_2O_5-WO_3-TiO_2 and alternative SCR catalysts in the abatement of VOCs, Catal. Today 53 (1999) 525–533, https://doi.org/10.1016/S0920-5861(99)00140-6.

[17] E. Finocchio, M. Baldi, G. Busca, C. Pistarino, G. Romezzano, F. Bregani, G. P. Toledo, Study of the abatement of VOC over V_2O_5-WO_3-TiO_2 and alternative SCR catalysts, Catal. Today 59 (2000) 261–268, https://doi.org/10.1016/S0920-5861(00)00292-3.

[18] S. Lomnicki, J. Lichtenberger, Z. Xu, M. Waters, J. Kosman, M.D. Amiridis, Catalytic oxidation of 2,4,6-trichlorophenol over vanadia/titania-based catalysts, Appl. Catal. B: Environ. 46 (2003) 105–119, https://doi.org/10.1016/S0926-3373(03)00215-7.

[19] C.E. Hetrick, J. Lichtenberger, M.D. Amiridis, Catalytic oxidation of chlorophenol over V_2O_5/TiO_2 catalysts, Appl. Catal. B Environ. 77 (2008) 255–263, https://doi.org/10.1016/j.apcatb.2007.07.022.

[20] M. Goemans, P. Clarysse, J. Joannès, P. De Clercq, S. Lenaerts, K. Matthys, K. Boels, Catalytic NO_x reduction with simultaneous dioxin and furan oxidation, Chemosphere 54 (2004) 1357–1365, https://doi.org/10.1016/S0045-6535(03)00255-8.

[21] L. Wang, W. Lee, P. Tsai, W. Lee, G. Chang-Chien, Emissions of polychlorinated dibenzo-p-dioxins and dibenzofurans from stack flue gases of sinter plants, Chemosphere 50 (2003) 1123–1129, https://doi.org/10.1016/S0045-6535(02)00702-6.

[22] M. Gallastegi-Villa, A. Aranzabal, J.A. González-Marcos, J.R. González-Velasco, Metal-loaded ZSM5 zeolites for catalytic purification of dioxin/furans and NO_x containing exhaust gases from MWI plants: effect of different metal cations, Appl. Catal. B Environ. 184 (2016) 238–245, https://doi.org/10.1016/j.apcatb.2015.11.006.

[23] M. Gallastegi-Villa, A. Aranzabal, J.A. González-Marcos, J.R. González-Velasco, Tailoring dual redox-acid functionalities in VO_X/TiO_2/ZSM5 catalyst for simultaneous abatement of PCDD/Fs and NO_X from municipal solid waste incineration, Appl. Catal. B Environ. 205 (2017) 310–318.

[24] J.A. Martín-Martín, M. Gallastegi-Villa, M.P. González-Marcos, A. Aranzabal, J. R. González-Velasco, Bimodal effect of water on V_2O_5/TiO_2 catalysts with different vanadium species in the simultaneous NO reduction and 1,2-dichlorobenzene oxidation, Chem. Eng. J. 417 (2021), https://doi.org/10.1016/j.cej.2021.129013.

[25] C. He, Y. Yu, Q. Shen, J. Chen, N. Qiao, Catalytic behavior and synergistic effect of nanostructured mesoporous CuO-MnO_x-CeO_2 catalysts for chlorobenzene destruction, Appl. Surf. Sci. 297 (2014) 59–69, https://doi.org/10.1016/j.apsusc.2014.01.076.

[26] F. Gao, X. Tang, H. Yi, S. Zhao, C. Li, J. Li, Y. Shi, X. Meng, A review on selective catalytic reduction of NO_x by NH_3 over Mn–based catalysts at low temperatures: catalysts, mechanisms, kinetics and DFT calculations, Catalysts 7 (2017) 1–32, https://doi.org/10.3390/catal7070199.

[27] M.S. Kamal, S.A. Razzak, M.M. Hossain, Catalytic oxidation of volatile organic compounds (VOCs) - a review, Atmos. Environ. 140 (2016) 117–134, https://doi.org/10.1016/j.atmosenv.2016.05.031.

[28] G. Picasso, M. Gutiérrez, M.P. Pina, J. Herguido, Preparation and characterization of Ce-Zr and Ce-Mn based oxides for n-hexane combustion: application to catalytic membrane reactors, Chem. Eng. J. 126 (2007) 119–130, https://doi.org/10.1016/j.cej.2006.09.005.

[29] H. Chen, A. Sayari, A. Adnot, F. Larachi, Composition-activity effects of Mn-Ce-O composites on phenol catalytic wet oxidation, Appl. Catal. B Environ. 32 (2001) 195–204, https://doi.org/10.1016/S0926-3373(01)00136-9.

[30] D. Delimaris, T. Ioannides, VOC oxidation over MnO_x-CeO_2 catalysts prepared by a combustion method, Appl. Catal. B Environ. 84 (2008) 303–312, https://doi.org/10.1016/j.apcatb.2008.04.006.

[31] H. Li, G. Lu, Q. Dai, Y. Wang, Y. Guo, Y. Guo, Efficient low-temperature catalytic combustion of trichloroethylene over flower-like mesoporous Mn-doped CeO_2 microspheres, Appl. Catal. B Environ. 102 (2011) 475–483, https://doi.org/10.1016/j.apcatb.2010.12.029.

[32] L. Xu, X. Li, M. Crocker, Z. Zhang, A. Zhu, C. Shi, A study of the mechanism of low-temperature SCR of NO with NH_3 on MnO_x/CeO_2, J. Mol. Catal. A Chem. 378 (2013) 82–90, https://doi.org/10.1016/j.molcata.2013.05.021.

[33] Q. Wang, X. Huang, Y. Feng, J. Zhou, H. Shi, J. Jin, Interaction mechanism study on simultaneous removal of 1,2-Dichlorobenzene and NO over MnO_x-CeO_2/TiO_2 catalysts at low temperatures, Ind. Eng. Chem. Res. 60 (2021) 4820–4830, https://doi.org/10.1021/acs.iecr.0c05862.

[34] J.A. Martín-Martín, M.P. González-Marcos, A. Aranzabal, J.R. González-Velasco, Effect of interaction degree between Mn and Ce of MnO_X-CeO_2 formulation on NO reduction and o-DCB oxidation performed simultaneously, J. Environ. Chem. Eng. 11 (2023) 110200, https://doi.org/10.1016/j.jece.2023.110200.

[35] A. Badri, C. Binet, J.-C. Lavalley, An FTIR study of surface ceria hydroxy groups during a redox process with H_2, J. Chem. Soc. Faraday Trans. 92 (1996) 4669–4673, https://doi.org/10.1039/FT9969204669.

[36] J.R. González-Velasco, J.A. Botas, J.A. González-Marcos, M.A. Gutiérrez-Ortiz, Influence of water and hydrocarbon processed in feedstream on the three-way behaviour of platinum-alumina catalysts, Appl. Catal. B Environ. 12 (1997) 61–79, https://doi.org/10.1016/S0926-3373(96)00058-6.

[37] A. BuzkováArvajová, J. Březina, R. Pečinka, P. Kočí, Modeling of two-step CO oxidation light-off on Pt/Γ-Al2O3 in the presence of C3H6 and NOX, Appl. Catal. B Environ. 233 (2018) 167–174, https://doi.org/10.1016/j.apcatb.2018.03.081.

[38] J. Brunet, E. Genty, C. Barroo, F. Cazier, C. Poupin, S. Siffert, D. Thomas, G. De Weireld, T.V. de Bocarmé, R. Cousin, The CoAlCeO mixed oxide: an alternative to palladium-based catalysts for total oxidation of industrial VOCs, Catalysts 8 (2018), https://doi.org/10.3390/catal8020064.

[39] M. Gallastegi-Villa, A. Aranzabal, M. Romero-Sáez, J.A. González-Marcos, J. R. González-Velasco, Catalytic activity of regenerated catalyst after the oxidation of 1,2-dichloroethane and trichloroethylene, Chem. Eng. J. 241 (2014) 200–206, https://doi.org/10.1016/j.cej.2013.12.008.

[40] Q. Ye, B. Xu, Textural and structure characterizations of Ce_{1-x} Mn_xO_2 prepared by citric acid sol-gel method, Acta Phys. Chim. Sin. 22 (2006) 345–349, https://doi.org/10.3866/PKU.WHXB20060318.

[41] J. Kan, L. Deng, B. Li, Q. Huang, S. Zhu, S. Shen, Y. Chen, Performance of co-doped Mn-Ce catalysts supported on cordierite for low concentration chlorobenzene oxidation, Appl. Catal. A 530 (2017) 21–29, https://doi.org/10.1016/j.apcata.2016.11.013.

[42] C.E. Hetrick, F. Patcas, M.D. Amiridis, Effect of water on the oxidation of dichlorobenzene over V_2O_5/TiO_2 catalysts, Appl. Catal. B Environ. 101 (2011) 622–628, https://doi.org/10.1016/j.apcatb.2010.11.003.

[43] X. Wang, Q. Kang, D. Li, Low-temperature catalytic combustion of chlorobenzene over MnO_x-CeO_2 mixed oxide catalysts, Catal. Commun. 9 (2008) 2158–2162, https://doi.org/10.1016/j.catcom.2008.04.021.

[44] R. Jokar, S. Mehdi Alavi, M. Rezaei, E. Akbari, Catalytic performance of copper oxide supported α-MnO_2 nanowires for the CO preferential oxidation in H_2-rich

stream, Int. J. Hydrogen Energy 46 (2021) 32503–32513, https://doi.org/10.1016/j.ijhydene.2021.07.108].
[45] M.A. Larrubia, G. Busca, An FT-IR study of the conversion of 2-chloropropane, o-dichlorobenzene and dibenzofuran on V_2O_5-MoO_3 -TiO_2 SCR-deNO_X catalysts, Appl. Catal. B Environ. 39 (2002) 343–352, https://doi.org/10.1016/S0926-3373(02)00116-9.
[46] E. Finocchio, G. Ramis, G. Busca, A study on catalytic combustion of chlorobenzenes, Catal. Today 169 (2011) 3–9, https://doi.org/10.1016/j.cattod.2010.10.097.
[47] L. Li, J. Shi, M. Tian, C. Chen, B. Wang, M. Ma, C. He, In situ fabrication of robust three dimensional ordered macroporous γ-MnO2/$LaMnO_{3.15}$ catalyst for chlorobenzene efficient destruction, Appl. Catal. B Environ. 282 (2021), https://doi.org/10.1016/j.apcatb.2020.119565.
[48] J. Zeng, X. Liu, J. Wang, H. Lv, T. Zhu, Catalytic oxidation of benzene over MnO_x/TiO_2 catalysts and the mechanism study, J. Mol. Catal. A Chem. 408 (2015) 221–227, https://doi.org/10.1016/j.molcata.2015.07.024.
[49] X. Weng, P. Sun, Y. Long, Q. Meng, Z. Wu, Catalytic oxidation of chlorobenzene over $Mn_xCe_{1-x}O_2$/HZSM-5 Catalysts: a study with practical implications, Environ. Sci. Tech. 51 (2017) 8057–8066, https://doi.org/10.1021/acs.est.6b06585.
[50] J. Lichtenberger, M.D. Amiridis, Catalytic oxidation of chlorinated benzenes over V_2O_5/TiO_2 catalysts, J. Catal. 223 (2004) 296–308, https://doi.org/10.1016/j.jcat.2004.01.032.
[51] Y. Gu, T. Cai, X. Gao, H. Xia, W. Sun, J. Zhao, Q. Dai, X. Wang, Catalytic combustion of chlorinated aromatics over WO_x/CeO_2 catalysts at low temperature, Appl. Catal. B Environ. 248 (2019) 264–276, https://doi.org/10.1016/j.apcatb.2018.12.055.
[52] Z. Zhang, J. Huang, H. Xia, Q. Dai, Y. Gu, Y. Lao, X. Wang, Chlorinated volatile organic compound oxidation over SO_4^{2-}/Fe_2O_3 catalysts, J. Catal. 360 (2018) 277–289, https://doi.org/10.1016/j.jcat.2017.11.024.
[53] X. Gao, X. Jiang, S. Shao, C. Tu, J. Pan, Y. Wang, H. Zhang, Q. Dai, L. Wang, X. Wang, Catalytic oxidation of chlorinated aromatics over Fe-based oxide catalysts modified by Mn, Chem. Eng. J. 446 (2022) 136771, https://doi.org/10.1016/j.cej.2022.136771.
[54] G. Wang, Y. Wang, L. Qin, B. Zhao, L. Guo, J. Han, Efficient and stable degradation of chlorobenzene over a porous iron-manganese oxide supported ruthenium catalyst, Catal. Sci. Technolog. 10 (2020) 7203–7216, https://doi.org/10.1039/d0cy01148g.
[55] J. Zhao, W. Xi, C. Tu, Q. Dai, X. Wang, Catalytic oxidation of chlorinated VOCs over Ru/Ti_xSn_{1-x} catalysts, Appl. Catal. B Environ. 263 (2020), https://doi.org/10.1016/j.apcatb.2019.118237.
[56] J. Wang, X. Wang, X. Liu, T. Zhu, Y. Guo, H. Qi, Catalytic oxidation of chlorinated benzenes over V_2O_5/TiO_2 catalysts: the effects of chlorine substituents, Catal. Today 241 (2015) 92–99, https://doi.org/10.1016/j.cattod.2014.04.002.
[57] Y. Gu, S. Shao, W. Sun, H. Xia, X. Gao, Q. Dai, W. Zhan, X. Wang, The oxidation of chlorinated organic compounds over W-modified Pt/CeO_2 catalysts, J. Catal. 380 (2019) 375–386, https://doi.org/10.1016/j.jcat.2019.06.041.
[58] Z. Zhang, H. Xia, Q. Dai, X. Wang, Dichloromethane oxidation over Fe_xZr_{1-x} oxide catalysts, Appl. Catal. A 557 (2018) 108–118, https://doi.org/10.1016/j.apcata.2017.12.003.
[59] F. He, Y. Jiao, L. Wu, X. Chena, S. Liu, Enhancement mechanism of Sn on the catalytic performance of Cu/KIT-6 during the catalytic combustion of chlorobenzene, Catal, Sci. Technol. 9 (2019) 6114–6123, https://doi.org/10.1039/c9cy01169b.
[60] B.H. Aristizabal, C. Montes de Correa, A.I. Serykh, C.E. Hetrick, M.D. Amiridis, In situ FTIR study of the adsorption and reaction of ortho-dichlorobenzene on Pd–Co sulfated zirconia catalysts, J. Catal. 258 (2008) 95–102, https://doi.org/10.1016/j.jcat.2008.06.001.
[61] Z. Xu, S. Deng, Y. Yang, T. Zhang, Q. Cao, J. Huang, G. Yu, Catalytic destruction of pentachlorobenzene in simulated flue gas by a V_2O_5-WO_3/TiO_2 catalyst, Chemosphere 87 (2012) 1032–1038, https://doi.org/10.1016/j.chemosphere.2012.01.004.
[62] Q. Jin, Z. Xue, X. Zhi, W. Ji, Y. Shen, Y. Zeng, Catalytic removal of NO and chlorobenzene over Ce-Mn-W-Zr-Ox/TiO2: performance study of hollow spheres effect, Fuel 305 (2021) 121534, https://doi.org/10.1016/j.fuel.2021.121534.
[63] F. Lin, Q. Wang, J. Zhang, J. Jin, S. Lu, J. Yan, Mechanism and kinetics study on low-temperature NH_3-SCR over manganese-cerium composite oxide catalysts, Ind. Eng. Chem. Res. 58 (2019) 22763–22770, https://doi.org/10.1021/acs.iecr.9b04780.
[64] X. Yu, X. Wu, Z. Chen, Z. Huang, G. Jing, Oxygen vacancy defect engineering in Mn-doped CeO_2 nanostructures for nitrogen oxides emission abatement, Mol. Cat. 476 (2019) 110512, https://doi.org/10.1016/j.mcat.2019.110512.
[65] M. Kantcheva, A. Agiral, O. Samarskaya, M. Stranzenbach, B. Saruhan, Characterization of $LaMnAl_{11}O_{19}$ by FT-IR spectroscopy of adsorbed NO and NO/O_2, Appl. Surf. Sci. 252 (2005) 1481–1491, https://doi.org/10.1016/j.apsusc.2005.02.139.
[66] M. Kantcheva, Identification, stability, and reactivity of NO_X species adsorbed on titania-supported manganese catalysts, J. Catal. 204 (2001) 479–494, https://doi.org/10.1006/jcat.2001.3413.
[67] T. Weingand, S. Kuba, K. Hadjiivanov, H. Knozinger, Nature and reactivity of the surface species formed after NO adsorption and NO+O_2 coadsorption on a WO_3–ZrO_2 catalyst, J. Catal. 209 (2002) 539–546, https://doi.org/10.1006/jcat.2002.3654.
[68] K.I. Hadjiivanov, Identification of neutral and charged N_xO_y surface species by IR spectroscopy, Catal. Rev.—Sci. Eng. 42 (2000) 71–144, https://doi.org/10.1081/CR-100100260.
[69] Y. Liu, T. Gu, X. Weng, Y. Wang, Z. Wu, H. Wang, DRIFT studies on the selectivity promotion mechanism of Ca-modified Ce-Mn/TiO_2 catalysts for low-temperature NO reduction with NH_3, J. Phys. Chem. C 116 (2012) 16582–16592, https://doi.org/10.1021/jp304390e.
[70] Z. Liu, Y. Yi, S. Zhang, T. Zhu, J. Zhu, J. Wang, Selective catalytic reduction of NO_X with NH_3 over Mn-Ce mixed oxide catalyst at low temperatures, Catal. Today 216 (2013) 76–81, https://doi.org/10.1016/j.cattod.2013.06.009.
[71] C. Yu, B. Huang, L. Dong, F. Chen, X. Liu, In situ FT-IR study of highly dispersed MnO_X/SAPO-34 catalyst for low-temperature selective catalytic reduction of NO_X by NH_3, Catal. Today 281 (2017) 610–620, https://doi.org/10.1016/j.cattod.2016.06.025.
[72] G. Gao, J. Shi, C. Liu, C. Gao, Z. Fan, C. Niu, Mn/CeO_2 catalysts for SCR of NO_X with NH_3 comparative study on the effect of supports on low-temperature catalytic activity, Appl. Surf. Sci. 411 (2017) 338–346, https://doi.org/10.1016/j.apsusc.2017.03.164.
[73] J. Li, H. Chang, L. Ma, J. Hao, R.T. Yang, Low-temperature selective catalytic reduction of NO_X with NH_3 over metal oxide and zeolite catalysts: a review, Catal. Today 175 (2011) 147–156, https://doi.org/10.1016/j.cattod.2011.03.034.
[74] G. Qi, R.T. Yang, Characterization and FTIR studies of MnO_X-CeO_2 catalyst for low-temperature selective catalytic reduction of NO with NH_3, J. Phys. Chem. B 108 (2004) 15738–15747, https://doi.org/10.1021/jp048431h.
[75] B.Q. Jiang, Z.B. Wu, Y. Liu, S.C. Lee, W.K. Ho, DRIFT study of the SO_2 effect on low-temperature SCR reaction over Fe-Mn/TiO_2, J. Phys. Chem. C 114 (2010) 4961–4965, https://doi.org/10.1021/jp907783g.
[76] C. Drouet, P. Alphonse, A. Rousset, IR spectroscopic study of NO and CO adsorptions on nonstoichiometric nickel-copper manganites, PCCP 3 (2001) 3826–3830, https://doi.org/10.1039/B101523K.
[77] K. Hadjiivanov, Use of overtones and combination modes for the identification of surface NO_X anionic species by IR spectroscopy, Catal. Lett. 68 (2000) 157–161, https://doi.org/10.1023/a:1019087521084.
[78] Q. Zhang, H. Wang, P. Ning, Z. Song, X. Liu, Y. Duan, In situ DRIFTS studies on CuO-Fe2O3 catalysts for low temperature selective catalytic oxidation of ammonia to nitrogen, Appl. Surf. Sci. 419 (2017) 733–743, https://doi.org/10.1016/j.apsusc.2017.05.056.
[79] F. Bertinchamps, M. Treinen, P. Eloy, A. Dos Santos, M.M. Mestdagh, E. M. Gaigneaux, Understanding the activation mechanism induced by NO_X on the performances of VO_X/TiO_2 based catalysts in the total oxidation of chlorinated VOCs, Appl. Catal. B Environ. 70 (2007) 360–369, https://doi.org/10.1016/j.apcatb.2005.11.022.
[80] Q. Wang, P.C. Hung, S. Lu, M.B. Chang, Catalytic decomposition of gaseous PCDD/Fs over V_2O_5/TiO_2-CNTs catalyst: effect of NO and NH_3 addition, Chemosphere 159 (2016) 132–137, https://doi.org/10.1016/j.chemosphere.2016.05.072.